UNIVERSIDADE ESTADUAL DE CAMPINAS
FACULDADE DE ENGENHARIA ELÉTRICA E DE COMPUTAÇÃO

Davi Marcelo Soares

Transition metal oxides and carbide as active electrodes for electrochemical capacitors

Óxidos de metais de transição e carbeto como eletrodos ativos para capacitores eletroquímicos

Campinas
2018

Davi Marcelo Soares

Transition metal oxides and carbide as active electrodes for electrochemical capacitors

Óxidos de metais de transição e carbeto como eletrodos ativos para capacitores eletroquímicos

Dissertation presented to the School of Electrical and Computer Engineering of the University of Campinas in partial fulfillment of the requirements for the degree of Master in Electrical Engineering, in the area of Electrical Energy.

Dissertação apresentada à Faculdade de Engenharia Elétrica e de Computação da Universidade Estadual de Campinas como parte dos requisitos exigidos para a obtenção do título de Mestre em Engenharia Elétrica, na Área de Energia Elétrica.

Supervisor/Orientador: Dr. Hudson Giovani Zanin

Co-supervisor/coorientador: Dr. Alfredo Carlos Peterlevitz

Este exemplar corresponde à versão final da dissertação defendida pelo aluno Davi Marcelo Soares, e orientada pelo Prof. Dr. Hudson Giovani Zanin.

Campinas
2018

Agência(s) de fomento e nº(s) de processo(s): CAPES

Ficha catalográfica
Universidade Estadual de Campinas
Biblioteca da Área de Engenharia e Arquitetura
Rose Meire da Silva - CRB 8/5974

So11t

Soares, Davi Marcelo, 1989-
Transition metal oxides and carbide as active electrodes for electrochemical capacitors / Davi Marcelo Soares. – Campinas, SP : [s.n.], 2018.

Orientador: Hudson Giovani Zanin.
Coorientador: Alfredo Carlos Peterlevitz.
Dissertação (mestrado) – Universidade Estadual de Campinas, Faculdade de Engenharia Elétrica e de Computação.

1. Capacitores. 2. Nióbio. 3. Tungstênio. I. Zanin, Hudson Giovani, 1983-. II. Peterlevitz, Alfredo Carlos. III. Universidade Estadual de Campinas. Faculdade de Engenharia Elétrica e de Computação. IV. Título.

Informações para Biblioteca Digital

Título em outro idioma: Óxidos de metais de transição e carbeto como eletrodos ativos para capacitores eletroquímicos
Palavras-chave em inglês:
Capacitor
Niobium
Tungsten
Área de concentração: Energia Elétrica
Titulação: Mestre em Engenharia Elétrica
Banca examinadora:
Hudson Giovani Zanin [Orientador]
Gustavo Doubek
Helder Jose Ceragioli
Data de defesa: 19-12-2018
Programa de Pós-Graduação: Engenharia Elétrica

Comissão Julgadora – Dissertação de Mestrado

Candidato: Davi Marcelo Soares **RA:** 208931

Data da defesa: 19 de Dezembro de 2018

Título da Tese: "Transition metal oxides and carbide as active electrodes for electrochemical capacitors"

Prof. Dr. Hudson Giovani Zanin (Presidente, FEEC/UNICAMP)
Prof. Dr. Gustavo Doubek (FEQ/UNICAMP)
Prof. Dr. Helder Jose Ceragioli (FEEC/UNICAMP)

A ata de defesa, com as respectivas assinaturas dos membros da Comissão Julgadora, encontra-se no processo de vida acadêmica do aluno.

Acknowledgments

I would like to express my sincere gratitude to all who helped me somehow to accomplish my masters degree studies.

Firstly, I would like to thank Dr. Hudson Giovani Zanin for his mentorship, and for always trusting me and introducing me to this field of research. Likewise, to Dr. Alfredo Carlos Peterlevitz for his patience, mentorship, wisdom, knowledge, and suggestions provided during this fruitful period at Carbon Sci-tech labs. *Paldies!*

Also, I appreciate Rafael Vicentini for providing samples, assisting me with electrochemical studies, and for his friendship; Dr. Helder Ceragioli for all knowledge and useful suggestions on hot filament chemical vapor deposition technique; Dr. Aline Pascon for allowing me to visit Center for Semiconductor Components (CCS) and for kindly helping me with scanning electron microscopy images; Willian Nunes for his suggestions regarding electrochemical impedance spectroscopy bibliography; Paloma for X-ray diffraction in samples and friendship; Dr. Elenice for assisting me with X-ray photoelectron spectroscopy spectra due to her expertise and friendship; Dr. Bruno Morandi for his revision and useful suggestions; Thais for assisting me with chemical synthesis and friendship; Bruno Freitas, Cesar, Carla, Carol, Lenon, Luiz Eduardo, Murilo, Otávio, Renato, Thayanne, Dr. Vera, and Vinícius for their friendship.

Special thanks to Dr. Cristiane Rodella for XRD diffraction at XPD beamline at Brazilian Synchrotron Light Laboratory (LNLS) , and to Dr. Leonardo Silva, from Federal University of Vales do Jequitinhonha e Mucuri (UFVJM), for his revision, suggestions and knowledge provided throughout my masters studies.

To Japanese government through Japan student services organization (JASSO) for financial support in the co-creative education program of humanities and sciences to solve global issues confronting Japan and Latin America (La-CEP) at Tokyo university of agriculture and technology (TUAT). Similarly, special thanks to Nanako Takase Sensei, Yoichi Tominaga Sensei, Kenzo Maehashi Sensei, Takashi Ikuta Sensei, and all students, who kindly accepted me for lab-work in their respective laboratories, allowing me to learn, feel part of their research groups, and showing me the unique Japanese culture.

More importantly, I appreciate the special support of my beloved wife Adriana, who encouraged me to pursue my masters and always had faith in myself, even during difficult times. Also, to my parents, sister and my niece Sarah.

This study was financed in part by the Coordenação de Aperfeiçoamento de Pessoal de Nível Superior - Brasil (CAPES) - Finance Code 001. The author also thank São Paulo Research Foundation (FAPESP), process 2014/02163-7, for financial support.

Dedication

I dedicate this study to my wife, my parents, my sister and my niece for their unconditional love, support, and source of encouragement.

But it is from the champions of the impossible rather than the slaves of the possible that evolution draws its creative force.
—Barbara Wootton

Abstract

The development of renewable energy storage systems is a cornerstone field for sectors such as electronics, aerospace and automobile. In research, techniques for producing efficient energy storage materials have drawn attention of researchers allover the world. Within this field, supercapacitors, also known as electrochemical capacitors, occupy special position, due to its high power density. This family of energy storage devices presents simple assembly, which is constituted by two electrodes – positive and negative terminals – an electrolytic medium, and a membrane, also known as separator, that plays the role of avoiding short circuit of positive and negative terminals, but allows ionic exchange in the electrolyte. Regarding the research efforts for supercapacitors, it is currently focused in the development of new electrode materials and electrolytes. For instance, within the materials tree for electrodes, transition metal oxides have called the attention due to faradaic or oxidation and reduction reactions. These reactions provide capacitance enhancement, but in most cases they do not allow long lifespan to the device. The purpose of this work is to present materials that have both redox reactions and longer lifespan. The two synthesized electrodes are namely: i) tungsten oxide (W_xO_y) and carbide W_2C composite, and ii) composite of multi wall carbon nanotubes (MWCNT) decorated with niobium pentoxide (Nb_2O_5). Both materials were grown by chemical vapor deposition (CVD) technique. Following the synthesis, characterization techniques were employed to evaluate the morphology, physical-chemical characteristics and electrochemical behavior of the composites. The experimental results of tungsten oxide and carbide show that the capacitance increased 119% during cyclability for Na_2SO_4 electrolyte. The efficiency also improved, from 59% at first cycle to 85% after 10,000 charge-discharge with constant current (GCD) cycles for Li_2SO_4 electrolyte. About the composite of MWCNT decorated with Nb_2O_5, the capacitance increased more than 34 times compared to an electrode made only out of MWCNT (without decoration). Therefore, the results reported herein present that both materials synthesized are candidates towards renewable supercapacitor devices, with Faradaic behavior and long lifespan.

Resumo

O desenvolvimento de sistemas de armazenamento de energias renováveis é um campo estratégico para setores tais como eletroeletrônico, aeroespacial e automotivo. Em pesquisa, técnicas para produção de materiais para armazenamento de energia eficiente tem sido objeto de estudos por grupos de pesquisa por todo o mundo. Neste âmbito, supercapacitores, também conhecidos como capacitores eletroquímicos, tem ocupado local de destaque, haja vista sua alta densidade de potência. Esta classe de armazenadores de energia tem por característica um processo relativamente simples de montagem, o qual constitui-se de dois eletrodos – terminais positivo e negativo – um meio eletrolítico, e um separador para impedir o curto circuito dos eletrodos mas permitir a troca iônica no meio eletrolítico. No tocante às linhas de pesquisa para capacitores eletroquímicos, muitos esforços tem sido colocados na busca por novos materiais de eletrodos e meios eletrolíticos. Por exemplo, no que se refere aos materiais para eletrodos, óxidos de metais de transição têm chamado atenção devido a ocorrência de reações faradáicas ou de oxi-redução. Tais reações proporcionam aumento na capacitância, mas na maioria dos casos não conferem ao dispositivo uma longa vida útil. O objetivo deste trabalho é apresentar dos compostos que possuem concomitantemente reações redox e longevidade na operação. Os dois materiais sintetizados são: i) composto de óxido (W_xO_y) e carbeto de tungstênio (W_2C), e ii) composto de nanotubos de carbono de paredes múltiplas (MWCNT) decorados com pentóxido de nióbio (Nb_2O_5) em substrato de alumínio com eletrodeposição de níquel. Os materiais sintetizados foram crescidos pela técnica deposição química em fase vapor (CVD). Posterior à síntese, técnicas de caracterização foram empregadas para avaliar a morfologia, características físico-químicas e comportamento eletroquímico dois compostos. Os resultados experimentais do dispositivo com eletrodo de óxido e carbeto de tungstênio mostram que a capacitância aumentou 119% ao longo da ciclabilidade para o eletrólito de Na_2SO_4. Já a eficiência também aumentou, de 59% no primeiro ciclo para 85% após 10.000 ciclos de carga e decarga com corrente constante (GCD) no eletrólito de Li_2SO_4. Quanto ao composto de MWCNT decorado com Nb_2O_5, a capacitância aumentou cerca de 34 vezes quando comparada com a de um eletrodo composto apenas por MWCNT. Portanto, os resultados expressos neste trabalho situam ambos os materiais sintetizados como candidatos para dispositivos supercapacitores com materiais ambientalmente sustentáveis, aliando características Faradáicas e longo ciclo de vida.

List of Figures

List of Tables

List of abbreviations

AC activated carbon.

CBMM Brazilian metallurgy and mining company.

CCS Center for Semiconductor Components.

CNT carbon nanotubes.

CPE constant phase element.

CV cyclic voltammetry.

CVD chemical vapor deposition.

DC direct current.

EC electrochemical capacitors.

EDL electric double layer.

EDLC electric double layer capacitor.

EIS electrochemical impedance spectroscopy.

ESI electrospray ionization.

ESR electric series resistance.

FAPESP São Paulo Research Foundation.

GCD galvanostatic charge-discharge.

HFCVD hot filament chemical vapor deposition.

HWCVD hot wire chemical vapor deposition.

JASSO Japan student services organization.

La-CEP co-creative education program of humanities and sciences to solve global issues confronting Japan and Latin America.

MWCNT multi wall carbon nanotubes.

SEM scanning electron microscopy.

TEM transmission electron microscopy.

TUAT Tokyo university of agriculture and technology.

UFVJM Federal University of Vales do Jequitinhonha e Mucuri.

XPS X-ray photoelectron spectroscopy analysis.

XRD X-ray diffraction.

Summary

Chapter 1

Introduction

Climate change and indiscriminate fossil fuel use are protagonists of ecologic and economic crises nowadays [11, 12]. Global warming is fact, regardless the reasons, and CO_2 emissions may be a reason for that. In order to control CO_2 emissions below the United Nations goal of 2 °C by 2050, one third of global oil reserves together with 50% and 80% of gas and coal reserves, respectively, must be kept intact for the next thirty five years [13, 14]. More than global warming, fossil fuels generate toxic sub-products such as sulfur dioxide (SO_2), nitrogen oxides (NO_x) and air particulate. These compounds pose as a direct threat to human health, and therefore represent a public health issue, as well [15, 16].

These and other facts have driven nations worldwide to encourage and invest in research and development of renewable energy sources, which neither generate toxic sub-products nor increase carbon emissions to atmosphere [17].

Such encouragement and incentives are translated into goals, for example the European union intends to have in its energy matrix renewable sources participation of 20% and 55% by 2020 and 2050, respectively. In addition, there are countries with a more aggressive policy, such as the United States, which intends to achieve 80% renewable sources by 2050; and Denmark, that foresees the abandon of all sources of fossil energy sources by 2050 [18]. Allied to the facts mentioned, renewable energy consumption nowadays is an indicative of economic growth. For this reason, development of these green energy sources is strategic towards nations development [19].

Nevertheless, development comes at a cost, which means that there are drawbacks that should be addressed when it comes to green sources [20]. One of the major obstacles lies in transport and direct supply to consumers; allied to the fact it cannot be produced on demand, e.g. conversion of solar energy during the night is impracticable. One alternative for these cited issues is the use of feasible electrochemical storage systems, such as batteries, electrochemical capacitors, or fuel cells. These storage devices play the role of supplying citizens and businesses during low generation and high demand periods (peak time). More importantly, due to environment-friendly nature of the generation, storage should attain

such feature, too [18, 21, 22].

Among the devices cited above, electrochemical capacitors – also known as supercapacitors, ultracapacitors or golden capacitors – have gained special position in the last ten years because their fast charge/discharge feature. Because lithium-ion batteries undergo through phase changes during its operation – which leads to low power delivery – they are deficient for applications that require fast charge/discharge. This niche of application is attractive to supercapacitors, once they present simple operating principle, high power supply capability, and longer life cycle (beyond 100,000 cycles) [11, 12]. These features and special position achieved are demonstrated by official statements given by governments around the world: e.g. United States Department of Energy attributed equal importance to supercapacitors and batteries for the future of energy storage systems. Likewise, currently there is an increasing volume of research – published papers, books, and patents – towards supercapacitors, as depicted by figure 1.1 [23].

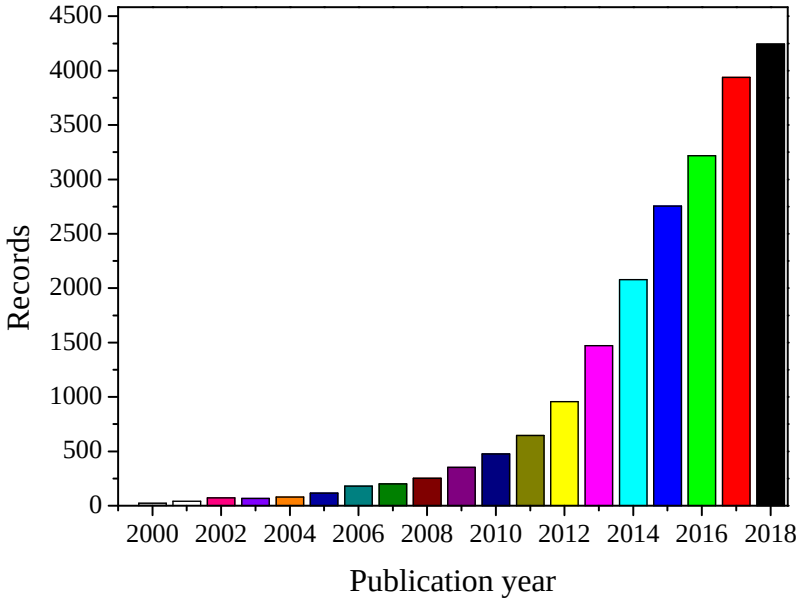

Figure 1.1: Number of records in articles, books, and authentic open literature related to supercapacitors from 2000 until 2018. Search formulation for "*supercapacitor*"; search from Web of Science; search time: 22, Jan, 2019.

This high volume of research, mainly focused in the pursuit of new materials, has lead to the development of different types of supercapacitor, as depicted in figure 1.2. According to figure 1.2, supercapacitors are divided in 3 main classes: i) electric double layer capacitors (EDLCs), ii) pseudocapacitors and iii) battery-like capacitors (hybrid systems). EDLCs are energy storage devices that store chemical energy by electrostatic adsorption of ions on electrode/electrolyte interface. Pseudocapacitors are EDLCs but with additional electron transfer across electrode/electrolyte interface [24]. Finally, battery-like capacitors, as name suggests, have charge discharge processes similar to battery at about constant voltage. In the latter case, electron transfer process is predominant on energy

storage mechanism. More details about supercapacitor features are provided on next chapter.

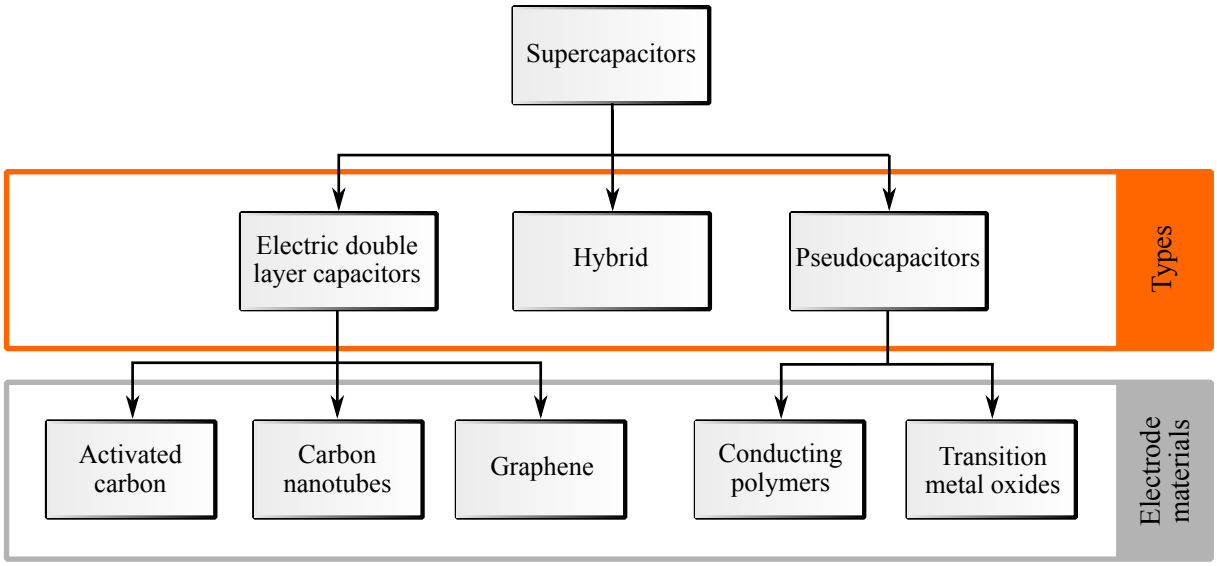

Figure 1.2: Supercapacitor classification for its different types. Adapted from [1].

It is also important to highlight that the prominent position achieved by supercapacitors is also due to the fact they are situated between batteries and capacitors, filling a gap between these two devices. This gap can be seen in the standard representation of power and energy for storage devices, known as Ragone plot, which is presented in figure 1.3. From Ragone plot, one is possible to compare different energy storage devices regarding their standardized power and energy values, as well as their discharge time – red lines.

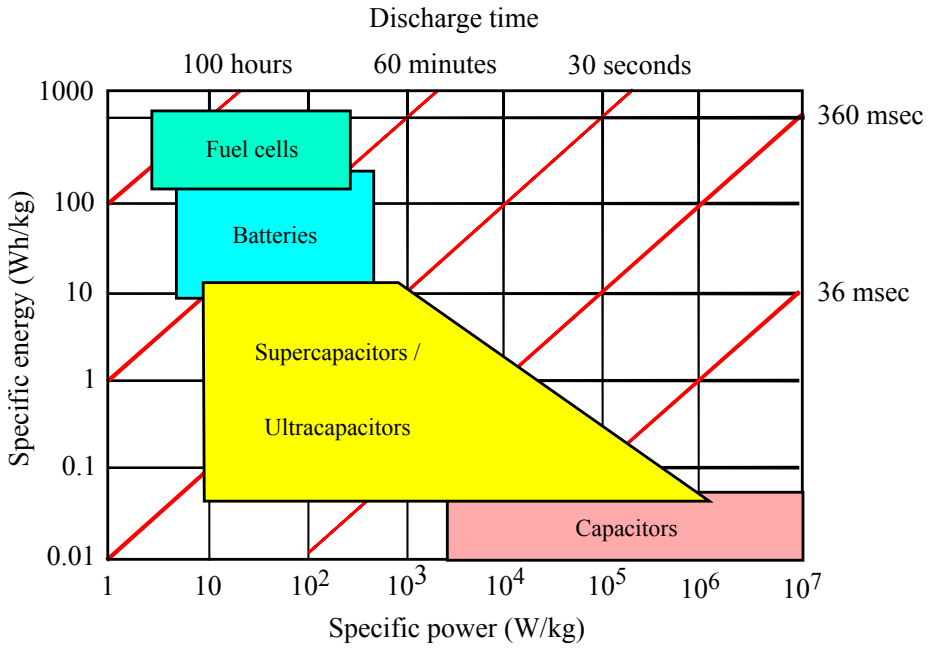

Figure 1.3: Ragone plot of energy storage systems.

Accordingly, it is possible to see, in terms of power and energy densities, that batteries have lower power but higher energy densities, the opposite of supercapacitors.

Aiming to contribute towards the development of environmentally friendly, low cost, safe, easily manufactured and long-life supercapacitors, this study presents the synthesis of two composite materials for electrodes. Both aggregated metal oxides, leading to pseudocapacitor type – as showed by figure 1.2.

Thus, at present work two new materials were developed using a technique known as chemical vapor deposition (CVD). Overall, besides developing materials with features above reported, the employed technique intends to show potential for large scale production.

Chapter 2

Capacitors

Capacitors are centennial energy storage devices. It is reported that in the mid-1700 at Leyden University, in the Netherlands, a device known as Leyden jar was capable to store energy [7].

This device was a jar coated with a thin silver foil internally and externally. As external part was grounded, it was possible to accumulate electric charges in the inner part of the jar through an electrostatic generator. Therefore, in this early capacitor it was possible to store energy energy – through electric charge accumulation – as well as to see electric discharges.

This primitive device gave rise to what would become one important devices for electronics concerning energy storage, electronic filters, and voltage divider for example. More than that, it preceded devices with higher power density to fill a gap within Ragone plot shown by figure 1.3. The theoretical principle of capacitors and supercapacitors is quite similar. More specifically, its equation starts with the device known as parallel plates capacitor.

2.1 Parallel plates capacitor

A capacitor is a device capable of accumulate electric energy in its electric field. Originally, this is composed by two parallel plates apart from a dielectric. The charge in the device accumulates when voltage is applied to its terminals, which forces positive and negative electric charges to accumulate on the terminals. Overall, a capacitor may provide electric current to a circuit for short periods of time. Its capacitance – given in Farad units – is the ratio of electric charge – given in Coulomb – which can be accumulated on the terminals for a voltage value – given in Volts. Hence, the capacitance of a capacitor obeys the equation 2.1.

$$C = \frac{Q}{V} \tag{2.1}$$

Moreover, for a capacitor with parallel plates, the capacitance is proportional to the area of the device, as well as to the material permittivity ($\varepsilon_0\,\varepsilon_r$). Similarly, the electric field in a double layer capacitor is given by the relation below.

$$E = \frac{\sigma}{\varepsilon_0\,\varepsilon_r} \tag{2.2}$$

$$\sigma = \frac{Q}{A} \tag{2.3}$$

Where, in equation 2.3 Q is the value of electric charge, in Coulomb, and A is the electrode surface area. The combination of equations 2.1, 2.2 and 2.3 yields equation 2.4

$$C = \frac{\varepsilon_0\,\varepsilon_r\,A}{d} \tag{2.4}$$

Where, ε_0 is permittivity of free space; ε_r is the relative material permittivity, and d is the distance between negative and positive terminals.

From conventional capacitors to supercapacitors few observations should be addressed, which are briefly covered here and in further details on the next section. In supercapacitors, capacitance may be from 3 to 10 orders of magnitude greater than conventional capacitors. Considering this information and equation 2.4, one way to achieve higher capacitance is by reducing the distance d, and/or by increasing surface area (A). The distance d on supercapacitors is equivalent to solvated ion radius on electrolyte, and not the distance between terminals or electrodes – as for conventional capacitors. Moreover, surface area on supercapacitors may range from hundred to thousand of m^2/g of active material. These facts corroborate to explain the greater values of capacitance of supercapacitors.

Regarding the energy stored in supercapacitors, commonly notations utilized are power density, or specific power, and energy density, or specific energy. These definitions take under consideration the mass of the electrode; therefore, normalizing the values for comparison purposes. The specific energy of supercapacitor is presented in the equation 2.5.

$$E = \frac{1}{2}\frac{C\,V^2}{m} \tag{2.5}$$

Where, in the equation 2.5, energy (E) is given in J, capacitance (C) in F, voltage applied to the terminals (V) in V; and m is the electrode mass, usually given in g.

Yet the specific power of a supercapacitor, according to the fundamental definition, is given by the rate of energy supplied to the load in time divided by the electrode mass, as stated by equation 2.6.

$$P = \frac{1}{m}\frac{\partial E}{\partial t} \tag{2.6}$$

As previously stated, one difference between capacitors and batteries is in terms of energy and power densities. Capacitors present higher specific power (higher than $5 \times 10^3\,\mathrm{W/kg}$); but lower specific energy (from 1×10^{-2} to $5 \times 10^{-2}\,\mathrm{W\,h/kg}$). Accordingly, compared to batteries, supercapacitors can be rapidly charged and discharged; despite its lower energy storage capacity [25].

2.1.1 Supercapacitors

Supercapacitors, also known as electrochemical capacitors, or ultracapacitors, are devices that store and supply energy, respectively, through rapid charge and discharge that happen on the electrode-electrolyte interface [7]. These devices are candidates for replacing batteries in applications that require high power and low weight. Due to their fast charge/discharge processes, supercapacitors can supply loads that require quick power bursts; therefore, with applicability that goes from wearable and mobile devices to automotive vehicles and aircrafts emergency doors [11, 26].

Other advantages of supercapacitors are their long durability and high efficiency, due to their mechanism of energy storage. For electric double layer capacitor (EDLC), one happens through electrostatic attraction of ions on electrode/electrolyte interface [7, 9]. activated carbon (AC) is the most employed material on EC electrodes due to its high surface area, which has impacts on capacitance magnitude, chemical stability, and low cost. Similarly, plenty of research has been done on carbon allotropes electrodes, namely, graphene, carbon nanotubes, and fullerenes, for instance [27].

Specifically about carbon nanotubes (CNT), that belong to the group known as 1D electrode materials, despite the fact they provide high electronic conductivity and path towards flexible devices, their specific surface area is considered low, usually below $200\,\mathrm{m^2/g}$ [28]. Notwithstanding, the surface capacitance of pristine carbonaceous films ranges from 5 to $15\,\mu\mathrm{F/cm^2}$, which may provide, depending on the electrolyte, a capacitance not higher than $200\,\mathrm{F/g}$, value also considered low by literature [29]. One alternative to overcome the low specific capacitance characteristic of pristine carbonaceous thin films is through the decoration with materials that may provide higher capacitance values. For instance, increase in capacitance may happen through faradaic or redox reactions. These reactions, also known as pseudocapacitance, may take place in devices that possess the following materials: carbons enriched in heteroatoms, conducting polymers, nanoporous carbons with electrosorbed hydrogen, and transition metal oxides [7]. Thus, deposition of such materials onto carbonaceous electrodes may be a successful approach towards higher capacitance devices [29, 30].

Hence, in supercapacitors there are two mechanisms in which charge is stored: electrostatic and faradaic. Regarding electrostatic mechanism, the majority of electrodes to that end are porous carbon allotropes [31–35]. However, as previously mentioned, limited

capacitance is achieved relying in the electrochemical double layer only, 100 - 200 F/g depending on the electrolyte [7, 31]. In order to overcome such limitation, transition metal oxides are one kind of materials that were employed at present study for achieving pseudocapacitive behavior [7].

As stated by equation 2.4, the pursuit for materials that provide high capacitance is mainly based on some variables expressed in that relation. For instance, high surface area materials are desired; reason why more than 90 % of commercial supercapacitors use carbon as the electrode active material [36]. Furthermore, the distance between the electrodes is related to the electric double layer thickness – for supercapacitors it has order of magnitude of angstrom (1×10^{-10} m). These few facts can bring useful information regarding the employed materials and operating principle of supercapacitors. For example, the double layer thickness shows why high power values can be achieved. Another reason for the high power lies in the fact that supercapacitors possess higher charge and discharge rates when compared to batteries. This fact is explained by the fact that these high reversible charge transfers and reactions do not promote phase changes or slow reactions at the electrode/electrolyte interface, like in batteries [7].

Apart from higher power density, supercapacitors also differ from batteries in the regard its life cycle – once some supercapacitors may achieve millions of cycles. Furthermore, supercapacitors present lower charge and discharge times, and higher efficiency – measured by the ratio of discharge and charge times – and by the fact that they can be completely charged and discharged without affecting its performance.

In relation to pseudocapacitance, it is typical of reactions in which electric charge (q) is proportional to change in potential ($\Delta\,\phi$), according to equation 2.1. Thus, pseudocapacitance, also known as faradaic or redox reactions, is usually achieved under following cases: i) surface redox in transition metal oxides or other materials; ii) ion intercalation that does not culminate in phase changes; iii) monolayer adsorption of ions in the electrode surface; iii) redox reactions in electrolytes at the electrode/electrolyte interface, for instance [37, 38]. The equation that rules such redox reactions is presented by equation 2.7.

$$\phi \approx \left(\frac{R\,T}{n\,F}\right) \ln\left[\frac{1}{1\,-\,q}\right] \tag{2.7}$$

Where, in equation 2.7, ϕ is voltage in V, R is the gas constant given in J/(mol K), T is the temperature in K, F is the Faraday constant, n is the number of electrons in the redox reaction, and q is the charge stored. This behavior is therefore named as pseudocapacitive as it is typical in capacitive charge/discharge processes [37].

It is also important to highlight that surface redox reactions exhibits kinetic that follows the equation 2.8.

$$i = C\,\nu \tag{2.8}$$

Where, in equation 2.8, i is the current in A, C is the capacitance given in F, and ν is the scan rate or sweep rate given in mV/s. In case a linear equation is obtained – as showed by equation 2.8 – the relation appears to be capacitive and this process is not diffusion limited but limited by surface processes. In the other hand, for processes limited by diffusion, the peak current is proportional to $\nu^{1/2}$. Thus, obeying the equation portrayed by equation 2.9.

$$i = C\,\nu^{1/2} \tag{2.9}$$

2.1.2 Physical based models of supercapacitors

The best known constructive principle of a supercapacitor is made out of two symmetrical – identical – electrodes placed in an electrolytic solution. In order to prevent short circuit of electrodes, a mesoporous membrane, also reported as separator – made out of paper, fiber glass, or polymer – is responsible for keeping the electrodes apart; but, allowing ion exchange between them [39].

By applying an external voltage to the terminals, ions in electrolytic solution, according to the natural principle of opposite polarity ion attraction as well as the diffusional process, will penetrate the mesoporous membrane towards their respective electrodes, where they will be adsorbed [25]. Figure 2.1 illustrates the processes of charge and discharge in supercapacitors.

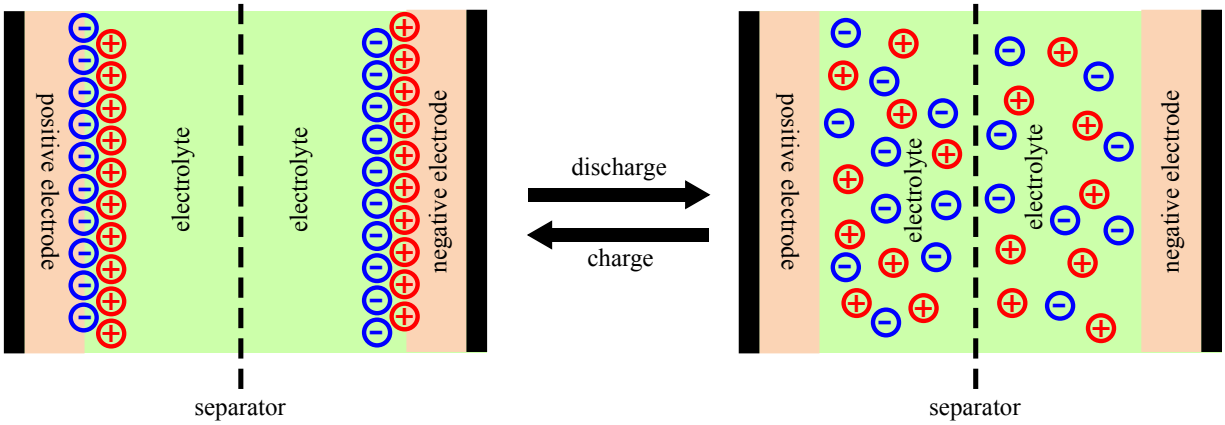

Figure 2.1: Charge and discharge mechanism in supercapacitors and ions disposition.

Electric double layer (EDLC) mechanism for supercapacitors

The electric double layer concept is the operating principle that supercapacitors present to store ions. This aspect can be modeled as a parallel plate capacitors separated

by a very small distance – factor of anstrom (1×10^{-10} m). This model was adopted by von Helmholtz to explain the distribution charges, as depicted in figure 2.2(a); and is known as double layer Helmholtz model [2].

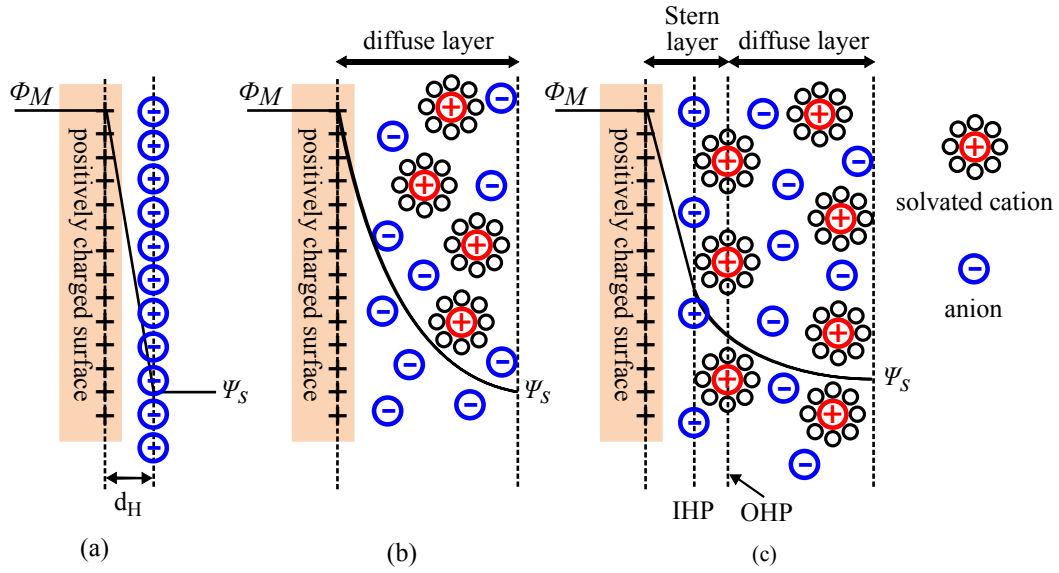

Figure 2.2: Electric double layer models on a positively charged surface: (a) Helmholtz model, (b) Gouy-Chapman model, and (c) Stern model. Adapted from [2].

Helmholtz model

The von Helmholtz model describes a capacitor according to its most fundamental relation, which means, two parallel plates separated by a known distance. On the positively charged plate surface there will be an anion absorbed layer, having its voltage profile linear, as presented by equation 2.10 [25].

$$C_H = \frac{\varepsilon}{d_H} \tag{2.10}$$

Where, d_H is the Helmholtz thickness layer, which has dimensions of solvated ions; and ε is the electric permittivity of the electrolyte. Figure 2.2(a) illustrates this model.

Although quite simple to visualize and understand, the Helmholtz model does not take into account the following aspects: ion diffusion, adsorption of them onto electrode surface, and interaction between solvent dipole moment, for instance. Therefore, due to the complexity of systems existent nowadays, more elaborated models are required.

Gouy-Chapman model

Due to the simplicity of Helmholtz model – which does not consider some physic parameters – a more elaborated model was conceived and is presented by figure 2.2(b).

This approach – Gouy-Chapman model – takes into account a continuous cation and anion distribution in the electrolyte under effect of ion thermal motion. This model, proposed by Louis Georges Gouy and David Chapman, also calls as *diffuse layer* the region where the ion concentration closer to the charged surface obeys Boltzmann distribution.

Although more elaborated than Helmholtz model, Gouy-Chapman overestimates the electric double layer capacitance, once it does not comprehend physical limitation for ions to get closer to electrodes, what does not possess physical meaning. Furthermore, the model considers ions as punctual charges. Treating ions like punctual charges means that the electric potential difference between the compact layer plane (ψ_a) and the metal with respect to electrolyte solution (ψ_M) is the same; also, it means the ion distribution goes further down to the metal substrate, where $d_H = 0$. Therefore, once the ions are very close to the surface the values of capacitance obtained theoretically are much higher than the real ones [2, 25]. This means that even though the Gouy-Chapman model had a more refined mathematical treatment, which involved Boltzmann's energy distribution equation and Poisson's relation, it was not enough due to serious overestimation of double-layer capacitance. Consequently, a more realistic model was then proposed by Stern.

Stern model

The drawback found in Gouy-Chapman model was overcame by Stern in the study published in *Zeitschrift fur Elektrochemie* in 1924, which contained a new theory for double-layers. One relevant aspect of Stern model is that it kept some contribution from previous models – Helmholtz and Gouy [2].

As introduced by figure 2.2(c), the model conceived an inner region of ions distribution, which obeys the Langmuir's adsorption isothermal curves. Beyond the inner region, there is the diffuse layer of ionic charge distribution – similar to Gouy-Chapman model. It is also important to highlight that in Stern model ions assume a finite size, which include their hydration shells.

As depicted in figure 2.2(c), in Stern model, the stern layer capacitance is in series with the diffuse layer capacitance. This equivalent circuit is similar to the one illustrated in figure 2.3.

Figure 2.3: Stern model circuit.

From figure 2.3, once the capacitors are in series, the equivalent of them will be analogous to resistors in parallel, as shown by equation 2.11.

$$\frac{1}{C} = \frac{1}{C_H} + \frac{1}{C_{diff}} \tag{2.11}$$

Where, in equation 2.11, C_H is the compact layer capacitance from Helmholtz; while, C_{diff} is the diffuse layer capacitance.

2.1.3 Usual techniques of electrochemical behavior characterization

When it comes to characterization techniques for supercapacitors, there are standard ones that are employed, and, therefore, widely reported in literature.

One relevant aspect is that even though supercapacitors may have different operating principle compared to electrostatic capacitors, they still being treated as parallel plates devices. Hence, surface area and thickness of the film, for instance, are parameters of interest when characterizing the devices.

The following topics present a brief explanation of some standard techniques employed for evaluation of supercapacitors electrochemical behavior and performance. The techniques discussed below were employed at the present study for the synthesized materials.

Cyclic voltammetry (CV)

One of the most employed techniques for electrochemical characterization is known as cyclic voltammetry (CV). According to its definition, in CV, the response current from the working electrode is obtained by applying a potential scan rate. This procedure thus allows to see the current that flows through the working electrode and counter electrode, or, in the two electrode system, from positive to negative terminals. The resulting plot is known as voltammogram, which is a standard plot of voltage in the x-axis versus current in the y-axis.

The response current is given in function of substrate material, electrolyte, and concentration of these. Furthermore, electrolyte oxidation and reduction reactions may occur at electrode/electrolyte interface. Then, such contribution, known as pseudocapacitance contribution, is usually identifiable in CV representation [4, 38].

Aiming to briefly show some theory behind a voltammogram, firstly we identify one recurrent nomenclature – *scan rate* (ν) – which is a potential constantly varying in time, with units given in V/s. By applying this potential rate, the voltage is presented by equation 2.12.

$$\phi = \nu\, t \tag{2.12}$$

Where ν is the scan rate in V/s; ϕ is the voltage in V; and t is time in s.

In order to clearly show the voltammetry principles, a simple RC circuit with a constant current source is used at the present topic. This circuit is introduced in figure 2.4, where C_d is the double-layer capacitance (EDLC), and R_s the internal equivalent resistance of the device.

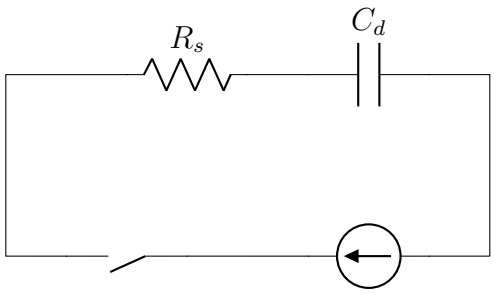

Figure 2.4: RC circuit with a constant current source.

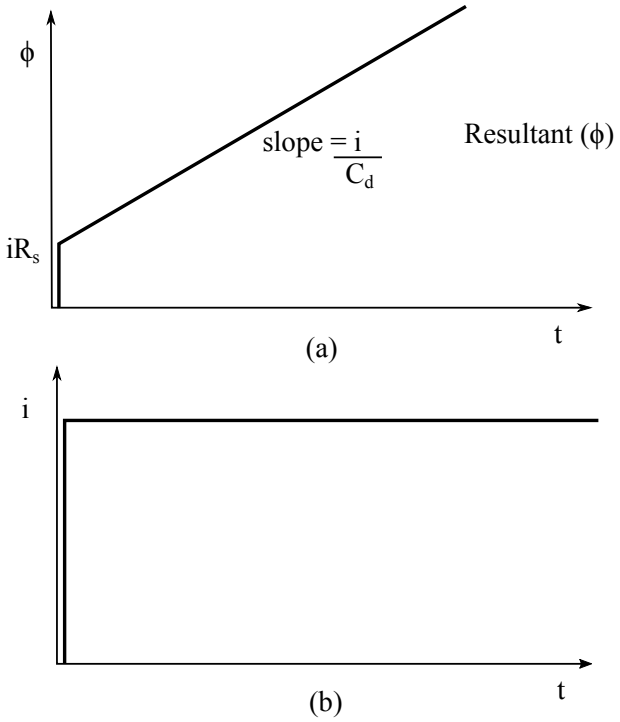

Figure 2.5: (a) Plot of voltage-time (ϕ-t) response of current step, considering that at $t = 0$ the capacitor C_d voltage is 0 V, (b) current step plot. Adapted from [3].

Supposing that the switch is closed at $t = 0$, and solving the circuit presented in figure 2.4 by applying the Kirchhoff's voltage law yields equation 2.13.

$$\nu\, t = R_s \left(\frac{dq}{dt}\right) + \frac{q}{C_d} \tag{2.13}$$

Setting the boundary conditions in equation 2.13 to $q = 0$ and t = 0, and summing the natural and forced responses of differential equation, yields equation 2.14.

$$i = \nu\, C_d \left[1 - \exp\left(\frac{-t}{R_s\, C_d}\right)\right] \tag{2.14}$$

From equation 2.13, the applied voltage increases linearly starting from iR_S at $t = 0$; whist in the capacitor (C_d) there is a voltage ramp sign starting from 0 V, as illustrated by figure 2.6(a). Furthermore, the current is presented in figure 2.6(b) obeys

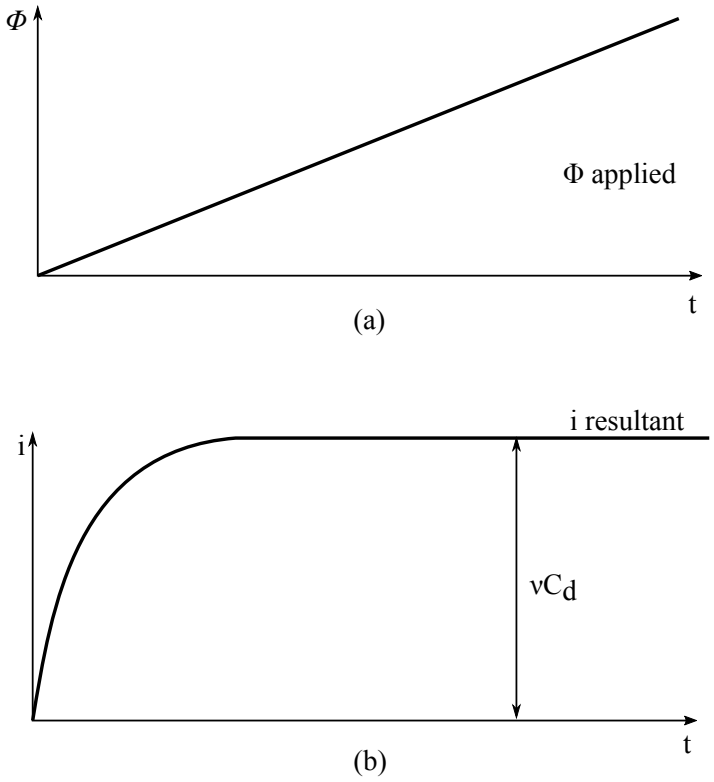

Figure 2.6: (a) Scan rate (ν) respresentation; (b) plot of current-time (i-t) result of increasing voltage application. Adapted from [3].

the relation presented in equation 2.15, once the derivative of the potential is constant.

$$i = C \frac{\mathrm{d}\,\phi}{\mathrm{d}\,t} \tag{2.15}$$

In equation 2.15, ϕ is the voltage, i is the current, and t is the time.

So far, we have covered only the positive derivative potentials for the voltammogram representation. It is now time to consider the negative derivative potentials, too, which are presented in figure 2.7(a). In the mentioned Figure, one is possible to visualize that the voltammogram presents a voltage decrease. Importantly, at the transition point there is a mathematical discontinuity, meaning that there is no derivative at that point. This fact is evidenced in figure 2.7(b) that shows the drop in the current curve – which is obtaining by taking the derivative of the potential – to zero.

Analogously to the positive cycle, the current versus time plot shows that at a certain point it reaches a constant value, also obeying the equation 2.15. The voltage versus current plot is illustrated by figure 2.7(c) – plot is known as voltammogram.

Finally, although it may look inconsistent at first moment placing a constant current source in order to obtain a voltage ramp in the capacitor C_d, for a RC series circuit, it is the best way to do that. At the circuit illustrated by figure 2.4, there is only one resistance (R_s). Nevertheless, in a real circuit, there are several distributed resistances, which lead to voltage drops along the circuit. These voltage drops may jeopardize the

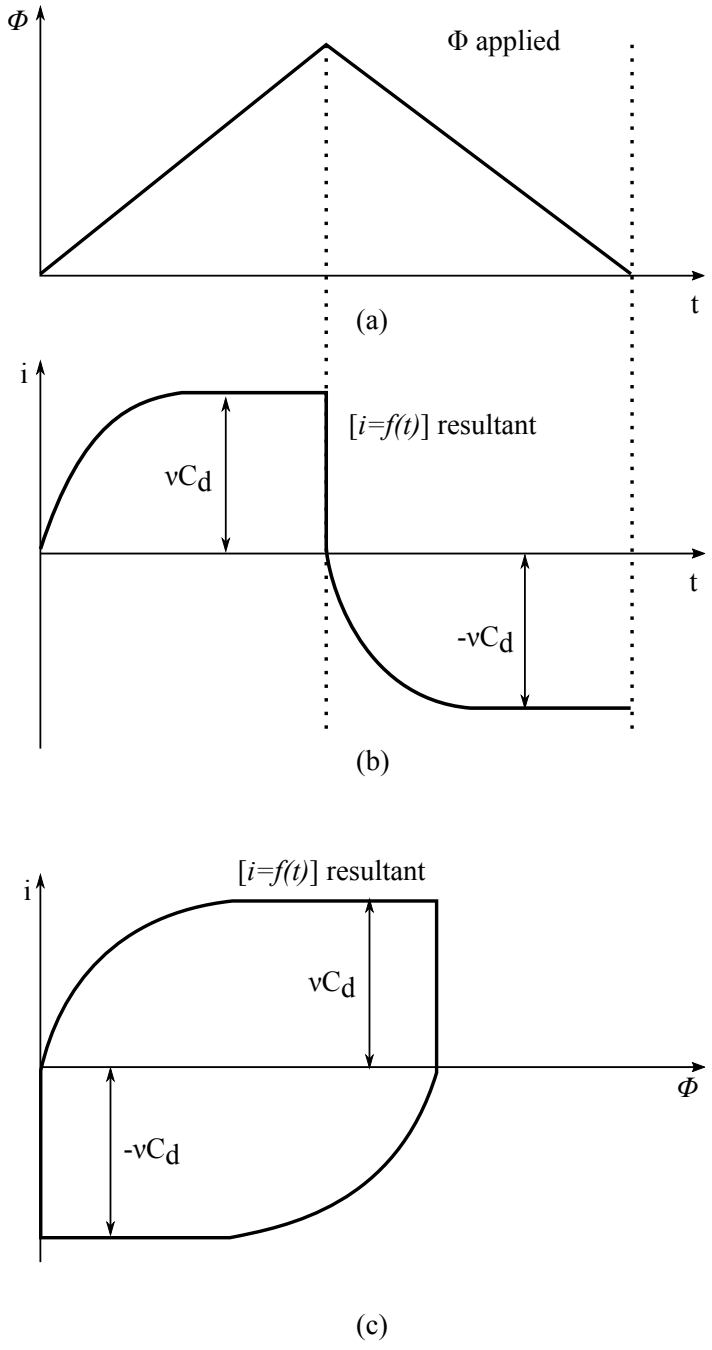

Figure 2.7: Plots of (a) triangular wave voltage applied for voltammetry, (b) current response in the capacitor device in function of time, and (c) response of current in function of voltage. Adapted from [3].

desired voltage signal at the capacitor C_d. This means that the voltage ramp in the capacitor – at rate ν – for a series RC circuit is harder to achieve when there is a voltage source in the circuit. Therefore, the best way to achieve that is by placing a current source in the circuit, as the voltage drops along the circuit will not change the desired voltage signal rate at the capacitor C_d.

Galvanostatic charge-discharge (GCD)

Galvanostatic charge-discharge is one of the most powerful tool to calculate capacitance and energy storage in devices. This technique, also called *chronopotentiometry*, analyzes the electric potential by applying a constant current previously set by the user. Given that the current is known and constant, the common representation of GCD is a plot of voltage versus time [4, 7]. Information such as capacitance, resistance, and performance of the device can be gathered by employing GCD [7].

When a direct current flows – electric charges in movement with frequency zero – accumulation of them happen on the electrode-electrolyte interface. This process, which obeys to equation 2.15, will provide voltage in the capacitor terminals during the time. Usually, a voltage quasi-triangular wave is observed, as portrayed by figure 2.8(a-b).

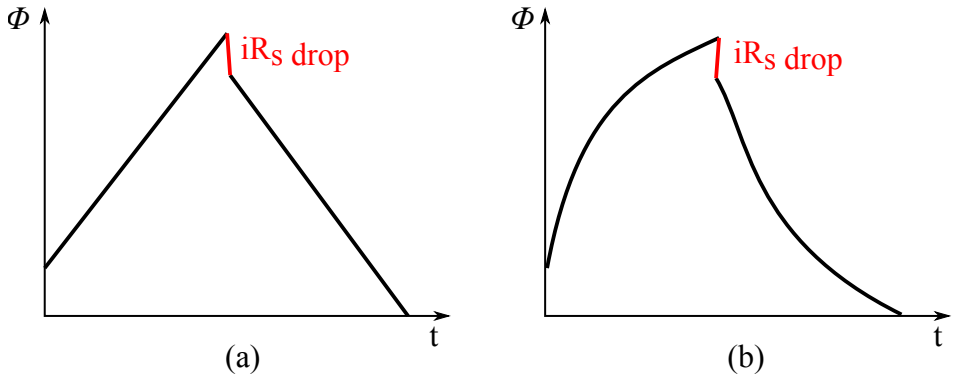

Figure 2.8: Galvanostatic charge-discharge typical voltage shapes, namely (a) linear, and (b) non-linear [4].

From GCD plot the capacitance of the device can also be calculated. This is performed through equation 2.16, presented below.

$$C = \frac{dq}{d\phi} \tag{2.16}$$

Where in equation 2.16 ϕ is the voltage, C is the capacitance and q is the electric charge. It is worth noting that q, in its differential form, is equals to equation 2.17.

$$dq = i\,dt \tag{2.17}$$

Replacing the differential term of 2.17 in equation 2.16, results in equation 2.18.

$$C = \frac{i\,\partial t}{\partial\,\phi} \tag{2.18}$$

Accordingly, from equation 2.18 it is possible to see that for obtaining the capacitance only two variables are required: current (i) and the variation of potential in time ($d\phi/dt$). In relation to current, in the galvanostatic case it is known. With respect to potential, for a supercapacitor, the voltage can be extracted from slope of the curve,

depicted in figure 2.8(a). While for a pseudocapacitor, as the voltage versus time curve is not linear as presented by figure 2.8(b), the capacitance is calculated by integrating the current either on charge or discharge time, as per equation 2.19 [4, 7].

$$C = \frac{1}{\Delta \phi} i \int dt \tag{2.19}$$

Where, in equation 2.19, $\Delta \phi$ is the voltage window, i is the known current, and dt is either the charge or discharge time.

Besides capacitance, another relevant property that is obtained through GCD plot is the supercapacitor efficiency. The relation that rules efficiency (η) is presented by equation 2.20.

$$\eta = \frac{t_{discharge}}{t_{charge}} \times 100\% \tag{2.20}$$

Where, $t_{discharge}$ and t_{charge} are the times of discharge and charge, respectively.

In terms of resistance of devices, the voltage drop – highlighted in red during current inversion in figure 2.8(a-b) – is related to the resistance of the cell. Therefore, it brings useful information regarding cell's performance.

Voltage drop is presented in equation 2.21.

$$R_s = \frac{\Delta \phi_{drop}}{\Delta i} \tag{2.21}$$

It is common when characterizing a device to keep track of the internal resistance evolution during time. It is made by repeatedly applying the equation 2.21. Thus, the GCD is used to cyclability evaluation, as well.

Electrochemical impedance spectroscopy (EIS)

Alternating current (AC) impedance spectroscopy, usually reported as electrochemical impedance spectroscopy, is the technique capable of evaluating a perturbation in a system upon applying a small magnitude AC signal. The measurements can be performed either at equilibrium state or with little displacement from it [4].

According to Ohm's law, the impedance of a circuit ($\dot{Z}$) is given by voltage divided by current. The equations 2.22 and 2.23 present the relations, respectively, for arbitrary AC voltage and current signals.

$$\phi(t) = V_0 \sin(\omega t) \tag{2.22}$$

$$I(t) = I_0 \sin(\omega t + \varphi) \tag{2.23}$$

Where, in equations 2.22 and 2.23, ω is the phase angle ($\omega = 2\pi f$); f is the

signal frequency given in Hz; and φ is the phase angle. For a pure capacitive current, it accounts for $\varphi = \pi/2$; whist for a pure resistive current it is equals to zero ($\varphi = 0$).

From the equation 2.22 presented, by varying the voltage wave sign frequency, its resulting value ($\phi(t)$) will also change; even though its maximum value is V_0. It happens because voltage value goes from -1 up to +1. The same principle applies for current signal ($I(t)$).

As a result, the EIS allows us to see the system behavior for a range of input signal frequencies. Results such as electric series resistance (ESR), charge transfer resistance, heterogeneous charge transfer parameters, and diffusion resistance can be quantified, along with the EDLC behavior [2–4, 39, 40].

The standard representation of EIS has two typical plots: frequency response plot, known as Bode plot, and Nyquist plot, in which real part is plotted in x-axis; while the imaginary part is plotted in y-axis [2]. The latter is illustrated in figure 2.10. As a matter of fact, the as called imaginary impedance, in case of a purely capacitive system, is given by equation 2.24.

$$\dot{Z_{im}} = -j\frac{1}{\omega\, C} = -j\frac{1}{2\pi\, f\, C} \tag{2.24}$$

Where, in equation 2.24, $j^2 = -1$. Furthermore, performing the proper mathematical steps in equation 2.24, it yields equation 2.25.

$$C = -j\frac{1}{\dot{Z_{im}}\, 2\pi\, f} \tag{2.25}$$

Nonetheless, differently from relation presented by equation 2.24, the impedance of a system hardly ever presents only capacitive part (Z_{im}). It means that the equivalent impedance of a system always have a resistive part (Z_{re}), too.

Although the applied signals in EIS are AC, which means they are frequency dependent, it is possible to analyze them using electrical circuits. Time dependent variables can be then studied in the frequency domain, and therefore be algebraically solved. This is one of the advantages of EIS. A simple typical circuit, known as simplified Randles cell, is presented in figure 2.9 [2].

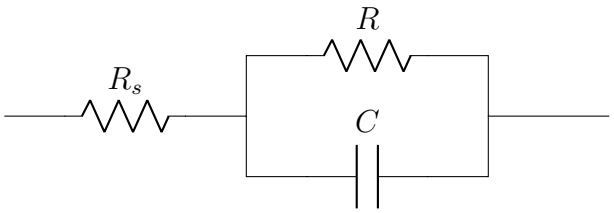

Figure 2.9: Simplified Randles cell for EIS.

From circuit depicted by figure 2.9, the equivalent impedance ($\dot{Z}$) is presented in equation 2.26.

$$\dot{Z} = R_s + \frac{R}{1 + j\,\omega\,R\,C} \tag{2.26}$$

From equation 2.26, there is a real component – denoted by Z_{re} – and a imaginary – denoted by Z_{im}. The total equivalent impedance ($\dot{Z}$) is given by the sum of Z_{re} and Z_{im}. The Nyquist representation on complex plane is presented by figure 2.10.

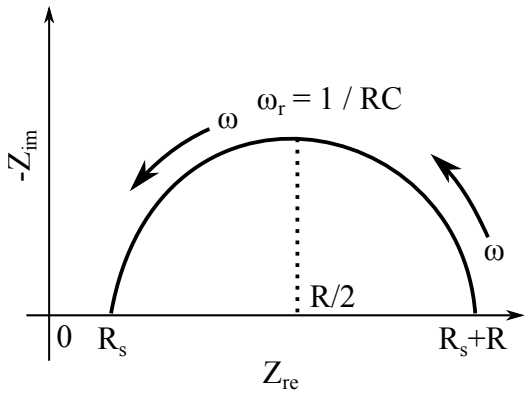

Figure 2.10: Nyquist impedance plot for simplified Randles' circuit presented by figure 2.9.

Furthermore, once the electric double layer (EDL) electrode/electrolyte interface nature is never purely capacitive, an approach known as CPE – which accounts for frequency dispersion at EIS – is commonly reported in literature. The capacitance frequency dispersion – which is presented by figure 2.11 – can be modeled by a distributed CPE, with impedance presented by equation 2.27.

$$\dot{Z_{CPE}} = \frac{1}{Y_0\,(j\,\omega)^{\alpha}} \tag{2.27}$$

Where in equation 2.27, Y_0 is the is the admittance modulus; ω is the angular frequency or signal pulsation ($\omega = 2\,\pi\,f$); and α is the dispersion coefficient [7, 41].

In particular, depending on the value of α there are three cases it is worth it to point out. For instance, by taking $\alpha = 0$ the equation 2.27 results in $\dot{Z_{CPE}} = 1/Y_0$; which is typical of a resistor, once there is no frequency dependence of such element. Yet when taking $\alpha = 1$, equation 2.27 results in $\dot{Z_{CPE}} = 1/(Y_0\,(j\,\omega))$, relation that corresponds to the capacitive reactance of a capacitor; thus, representing a purely capacitive element, as introduced by equation 2.24. In the other hand, by taking $\alpha = 1/2$ yields $\dot{Z_{CPE}} = 1/(Y_0\,(j\,\omega)^{1/2})$, behavior that is reported by literature as *Warburg* element, and accounts for the system polarization due to diffusion limitation impedance. One example of electric circuit with CPE – employed for fitting EIS at present study – is depicted in figure 2.11.

Where, in figure 2.11 R_s is the equivalent series resistance; R_{ct} is the charge-transfer resistance; $C_{CPE_{EDL}}$ is the capacitance of double-layer; and C_{CPE_θ} is the capacitance related to the pseudocapacitive reactions [5]. Typical shapes of a Randles's circuits

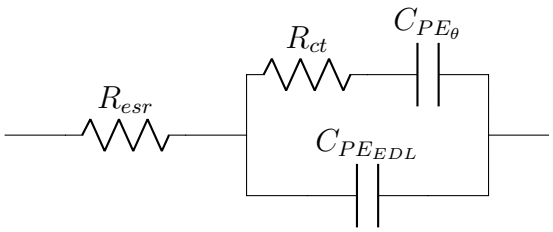

Figure 2.11: Example of Randles' circuit with CPE for EIS fitting [5, 6].

are portrayed in figure 2.11, where $\alpha = 1$ (red dashed line) and $\alpha = 0.5$ (black dashed line).

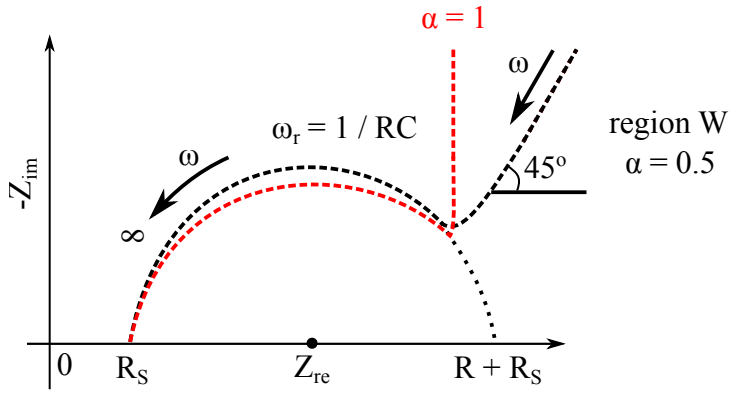

Figure 2.12: Typical Nyquist plot for a pseudocapacitor with a CPE element. Adapted from [7].

In sum, EIS is nowadays one of the most promising techniques for providing further information regarding materials, as well as for better grasping processes that take place within electrolyte and electrode-electrolyte interface [42]. The following studies present EIS aiming to further elucidate de electrochemical aspects of the synthesized materials.

Chapter 3

Tungsten oxide and carbide as active materials for electrochemical capacitors

3.1 Introduction

Tungsten carbide is the material, since the 1960s, most employed for catalytic reactions due to its low cost and ability to not be poisoned by H_2S and CO species, for example. Besides extensively studied for catalytic reactions, its low cost, corrosion resistance, and catalytic ability – analogous to noble metals – make it a candidate to renewable energy storage applications [43–45]. Likewise, the other species of interest at the present study, tungsten trioxide (WO_3), exhibits chemical stability, various morphologies, low cost, electrochromic and gaschromic properties [46–48]. Similarly, tungsten oxide is a promising material for field-emission, solar energy and energy storage [49]. As a consequence, capacitive behavior of tungsten oxide WO_3 has been reported by literature through several methods, such as microwave-assisted, electrochemical deposition, hydrothermal preparation and precipitation method [48, 50–53].

However, with relation to supercapacitors, the main issue of tungsten oxides (W_xO_y) is their lack for chemical stability, yielding low lifespan devices. For the best of our knowledge, the longest reported cyclability of WO_3 electrode is 5,000 cycles, with capacitance retention of 87% [54].

To overcome this issue, this study grew two main species of tungsten for supercapacitor electrodes: i) WO_3, which provides pseudocapacitive behavior; and ii) W_2C, which is a very stable tungsten alloy in aqueous media.

In this study, W_2C was synthesized onto copper substrate, as copper does not react with tungsten, but they form what is called "*pseudoalloy*", once their mutual solubility is negligible. Furthermore, they combine the desirable properties of electrical contact for their use as electrodes [55]. More importantly, to the best of our knowledge, there is no study published yet that synthesized W_2C combined with tungsten oxide species (W_xO_y)

on copper substrate and characterized it as supercapacitor.

In relation to carbon, which is part of the W_2C molecule, it comes from the as-purchased tungsten wires – which is coated by carbon layer – and also from vacuum pump oil [56]. In any case carbon may evaporate to surface and diffuse. Carbon may also spontaneously adsorb on surfaces, forming a film known as adventitious carbon [56]. This adsorbed carbon may also lead to the production of new species.

With respect to the technique employed in the present work for depositing a thin tungsten film onto copper substrate hot filament chemical vapor deposition (HFCVD), also known as hot wire chemical vapor deposition (HWCVD), was employed. At HFCVD, catalytic decomposition of hydrogen gas in atomic hydrogen happens by decomposing the gas molecules to radical species once they hit the tungsten hot filament. Therefore, the film formation occurs due to concomitant chemical reactions such as etching by the atomic hydrogen generated, gas phase chemistry, and the thin film deposition itself, among others [57–60]. Furthermore, at HFCVD, the pressure during the growth process is low, around 1 Pa, similar to sputtering technique, which, therefore, considerably avoids the formation of dust and particles accumulation on the substrate. It is worth noting also that besides the reduced number of particles, the films obtained have lower stress, opposite to the plasma assisted depositions, for instance [57]. Nonetheless, the presence of O_2 during the deposition, even under low pressure, induces at some degree oxidation on the film [46].

Our technique is fast, low cost, very reproducible, and environment-friendly. Also, this technique does not require any typical carbon-containing gas, such as methane (CH_4), ethane (C_2H_6), butane (C_4H_{10}), and carbon monoxide (CO), which can be either expensive or toxic [61].

Lastly, we report here a coin cell device assembled with W_2C and W_xO_y composite as active electrode for electrochemical capacitor, henceforth referred as W_2C:W_xO_y composite. The composite thin film shows chemical stability, long lifespan, and higher capacitance due to pseudocapacitive behavior.

3.2 Experimental procedures

Samples of polycrystalline copper were mechanically polished (1200 and 2000 grit) using sandpaper and then placed in sonication for 10 minutes in a solution containing 99.5% Synth ethyl alcohol for organic cleaning. Afterwards, samples were dried and transferred into HFCVD reactor for the deposition.

The HFCVD reactor consisted of a stainless steel chamber, whose volume corresponded to approximately 20 L and base pressure of 5.8×10^{-3} mbar. Thus, small quantities of oxygen and water vapor were presented in this configuration. Two tungsten filaments of diameter 236 μm were equally 80 mm long; both positioned approximately 10 mm above the substrate holder. Figure 3.1 shows an schematic of this technique. During

evaporation process, 50 sccm of H_2 was flowed into the chamber; and that was the only gas flowed during sample preparation. H_2 gas was employed aiming to provide a reducing environment by removing oxygen from the copper surface. Catalytic decomposition of hydrogen gas in atomic hydrogen happens by decomposing H_2 gas molecules to radical species due to contact with hot tungsten wires.

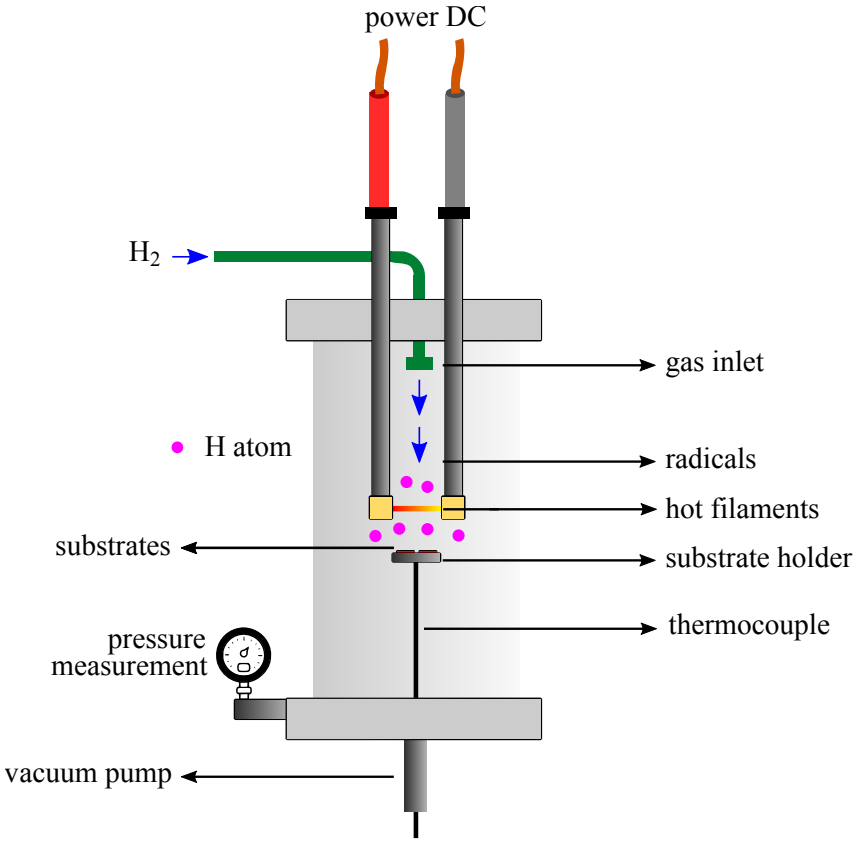

Figure 3.1: Representation of HFCVD reactor principle. Adapted from [8].

After the growth process, which took 10 min at 425 °C, samples were removed from the HFCVD chamber and exposed to room temperature. After that, electrochemical capacitors were assembled using the as-grown substrates as working electrodes according to the assembly steps portrayed by figure 3.2. In addition, all reagents used in this experiment were guaranteed-grade and used without further purification procedures.

3.3 Materials characterization

Morphology and structure were investigated by scanning electron microscopy (SEM) and transmission electron microscopy (TEM), respectively. FEI Nanolab 200 and JEOL 2100 MSC microscopes were employed. Chemical bonding and vibrational modes were investigated by Raman spectroscopy, which was performed by Renishaw inVia with laser Ar^+ of 2.41 eV (514.5 nm). X-ray diffraction using synchrotron source was performed at Brazilian Synchrotron Light Laboratory (LNLS) at XPD beamline with wavelength of

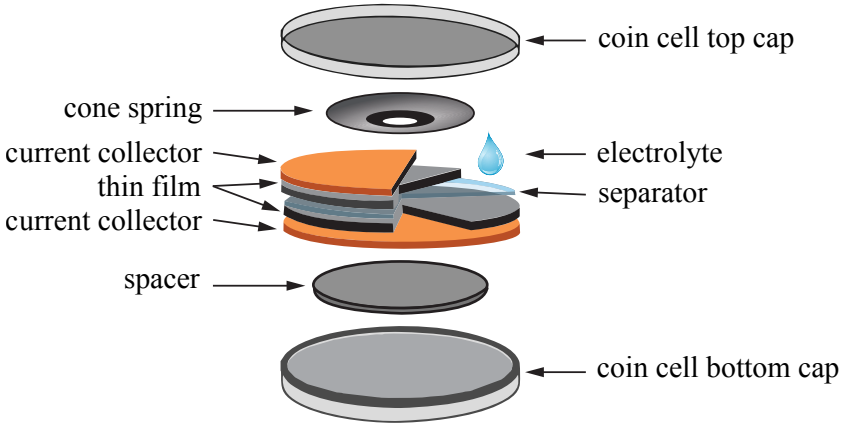

Figure 3.2: Representation of coin cell assembly and its components used in the present study.

1.6531 Å (7.5 keV) and a linear detector Mythen-1K installed 1 m from the sample. Also, XPS spectra were taken by Thermo K-α XPS, monochromatic small-spot, Al anode, (hν = 1486 eV), spot 400 μm.

3.4 Devices characterization

Electrochemical characterization was accomplished using the Interface 1010E potentiostat-galvanostat from Gamry. The two-electrode system was assembled using a 2032-coin cell, as presented in figure 3.2. All experiments were performed using the W_2C:W_xO_y composite as electrodes separated by a mesoporous cellulosic membrane, one device soaked with 1 mol/l Li_2SO_4 and another with 0.5 mol/l Na_2SO_4 electrolytic solutions. Cyclic voltammetry (CV) was performed from 5 to 100 mV/s; galvanostatic charge/discharge (GCD) was carried out at 120 µA; and electrochemical impedance spectroscopy (EIS) was performed at 250 mV with amplitude of 10 mV from 0.10 Hz up to 10 kHz.

3.5 Results and discussion

3.5.1 Morphology

SEM and TEM microscopies are presented in figure 3.3(a-i). Figure 3.3(a-g) evidences that the W_2C:W_xO_y composite has homogeneous porous surface; while figure 3.3(h-i) confirms that there are tungsten carbide nanoparticles – dark contrast – with particles ranging from $\approx$ 2 nm to $\approx$ 10 nm. These features are aspects of interest for electrodes of electrochemical capacitors, once they provide homogeneous and higher surface area electrodes, which theoretically leads to higher capacitance values as shown by equation 2.4.

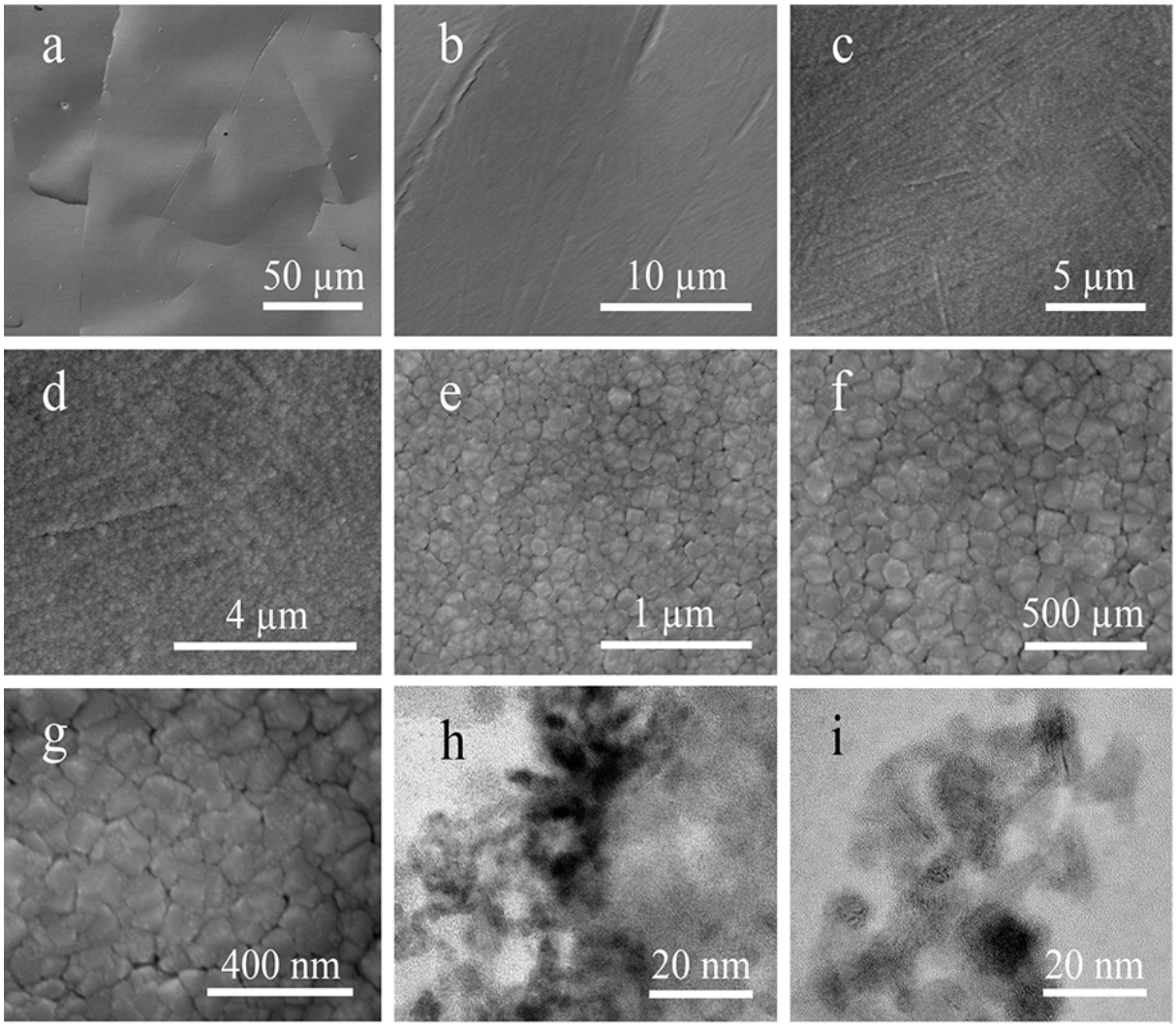

Figure 3.3: (a-g) SEM and (h,i) TEM data took from W_2C:W_xO_y composite.

3.5.2 Raman spectroscopy

Figure 3.4(a) shows the Raman spectra of W_2C:W_xO_y composite, where the phonon activity is represented in two broader bands. Firstly, it is not observed many peaks within the low-frequency range (lower than $200\,cm^{-1}$), which corresponds to the lattice vibration modes. The first band lies within the range of 200 - $500\,cm^{-1}$, showing O – W – O bending modes characteristic. [62] Peaks within Raman shift 200 - $500\,cm^{-1}$ present component curves at $\approx 220\,cm^{-1}$, which is assigned to bending of the dangling oxygen and O – W – O stretching. [63, 64] Bands ranging from 600 to $1000\,cm^{-1}$ in figure 3.4(a) are assigned to stretching modes of O – W – O, such the one highlighted at $620\,cm^{-1}$. [46, 62, 63, 65] Furthermore, in figure 3.4(a,b), the identified D and first-order G bands are characteristic of sp^2 carbon materials, where D stands for defected-activated Raman mode, and G for graphitic.

In order to identify origin of carbon on W_2C:W_xO_y composite, extended spectrum of the tungsten filament used in the sublimation procedure is investigated and presented

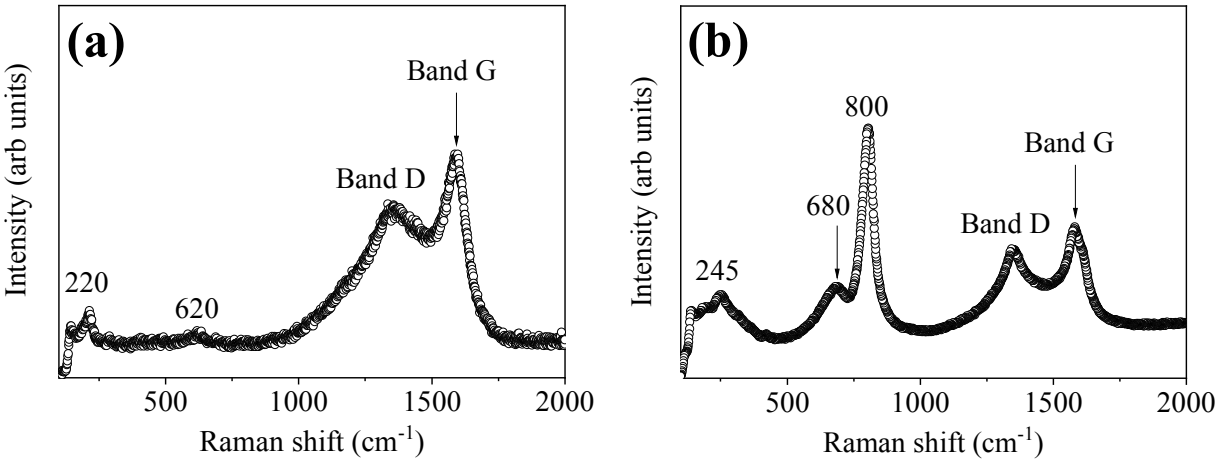

Figure 3.4: Raman spectra of (a) W_2C:W_xO_y thin film, and (b) as-purchased tungsten filament.

in figure 3.4(b). The peaks presented are partially similar to the WO_3 spectrum adding amorphous carbon peaks related to mainly D, G and G'. Peak located at approximately $165\,cm^{-1}$ is attributed to stretching and deformation modes. Whereas, the peak located at $257\,cm^{-1}$ is characteristic of δ (O-W-O) bending vibration, indicating WO_3 crystalline [66]. Peaks centered at about $805\,cm^{-1}$ and $700\,cm^{-1}$ are typically assigned to O – W – O modes. Combination of all these features is typical of monoclinic WO_3 [66–68].

In relation to carbon species, peaks at $1350\,cm^{-1}$ and $1580\,cm^{-1}$ are known as D and G bands, respectively, and typical bands of carbon hybridization. The D band is assigned to sp^2 hybridized carbon disorder; whilst the G band is assigned to C – C bond stretching in sp^2 hybridized carbon materials. Likewise, in respect to the broader bands after these peaks – higher than $2000\,cm^{-1}$ – they are known as second order graphite peaks [64]. Therefore, this characterization in the tungsten filament corroborates to ascertain our preliminary idea, i.e. the carbon within carbide molecule may come also from the filament.

3.5.3 X-ray diffraction (XRD)

Figure 3.5 presents XRD patterns for 2θ from 35° to 76°. The crystal phase formed for tungsten carbide is identified as trigonal W_2C. It is assigned to peaks (0 0 2), (1 1 1), (1 1 2), and (1 1 3) [69]. In the other hand, the two more intense peaks – with hkl-planes (1 1 0) and (2 0 0) – respectively located at 43.1° and 62.9° are assigned to metallic tungsten with cubic crystal phase [70]. Lastly, two less intense peaks assigned to WO_3 are located at 36.94° and 66.56°, with peaks at (2 2 0) and (4 -2 2), and identified as triclinic [71].

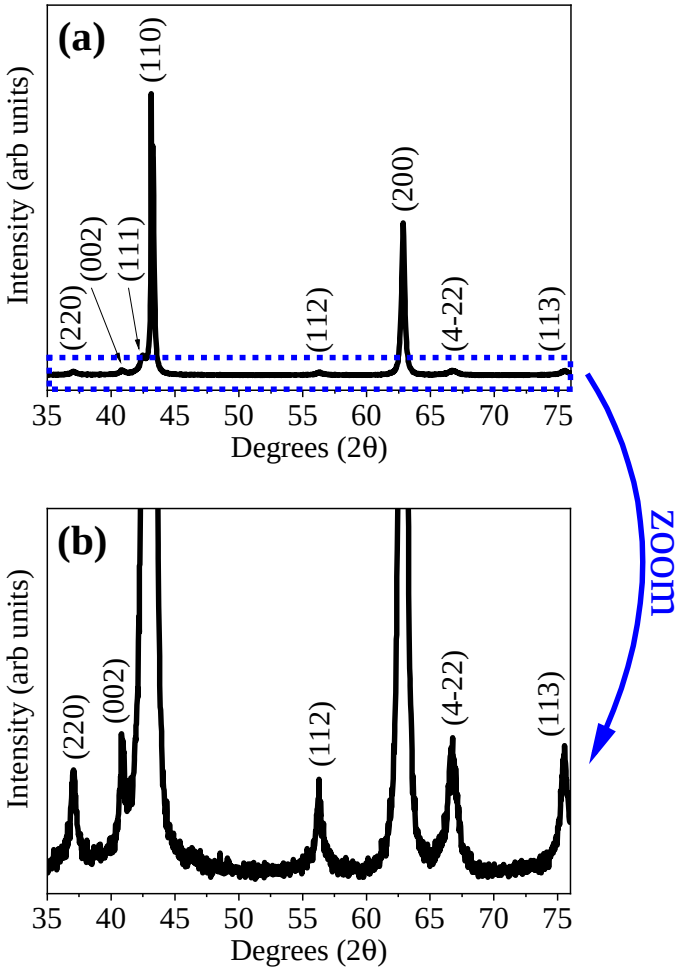

Figure 3.5: (a)XRD pattern of W_2C:W_xO_y composite, (b)pattern of small intensity peaks.

3.5.4 X-ray photoelectron spectroscopy analysis (XPS)

XPS spectra are presented in figure 3.6(a-d). The spectrum known as long scan – depicted in figure 3.6(a) – shows the elemental components, which are detailed herein. According to spectrum presented in figure 3.6(b), at $W4f_{7/2}$ there is a peak in 31.6 eV assigned to WC phase. Furthermore, there is another W4f spin-orbit component ($W4f_{5/2}$) located at 33.8 eV, which indicates the presence of carbide, due to C – W bonds, which means W_2C or WC [72–75].

Yet the $W4f_{7/2}$ peak at 35.78 eV is characteristic to tungsten six-valent state (W^{6+}), in accordance, with the reference value 35.7 eV. Likewise, the peaks at 35.9 eV ($W4f_{7/2}$) and 38 eV ($W4f_{5/2}$) are related to tungsten oxide; the latter is characteristic of W^{6+} state [76–80].

Accordingly, it is possible to claim that there is WO_3 and metallic tungsten in the composite [55]. The chemical shift of WO_3 and metallic W is 4.2 eV. As a matter of fact, the double-peak structure due to $W4f_{7/2}$ and $W4f_{5/2}$ states is $\approx$ 2.15 eV, both results in accordance with literature results [79–82].

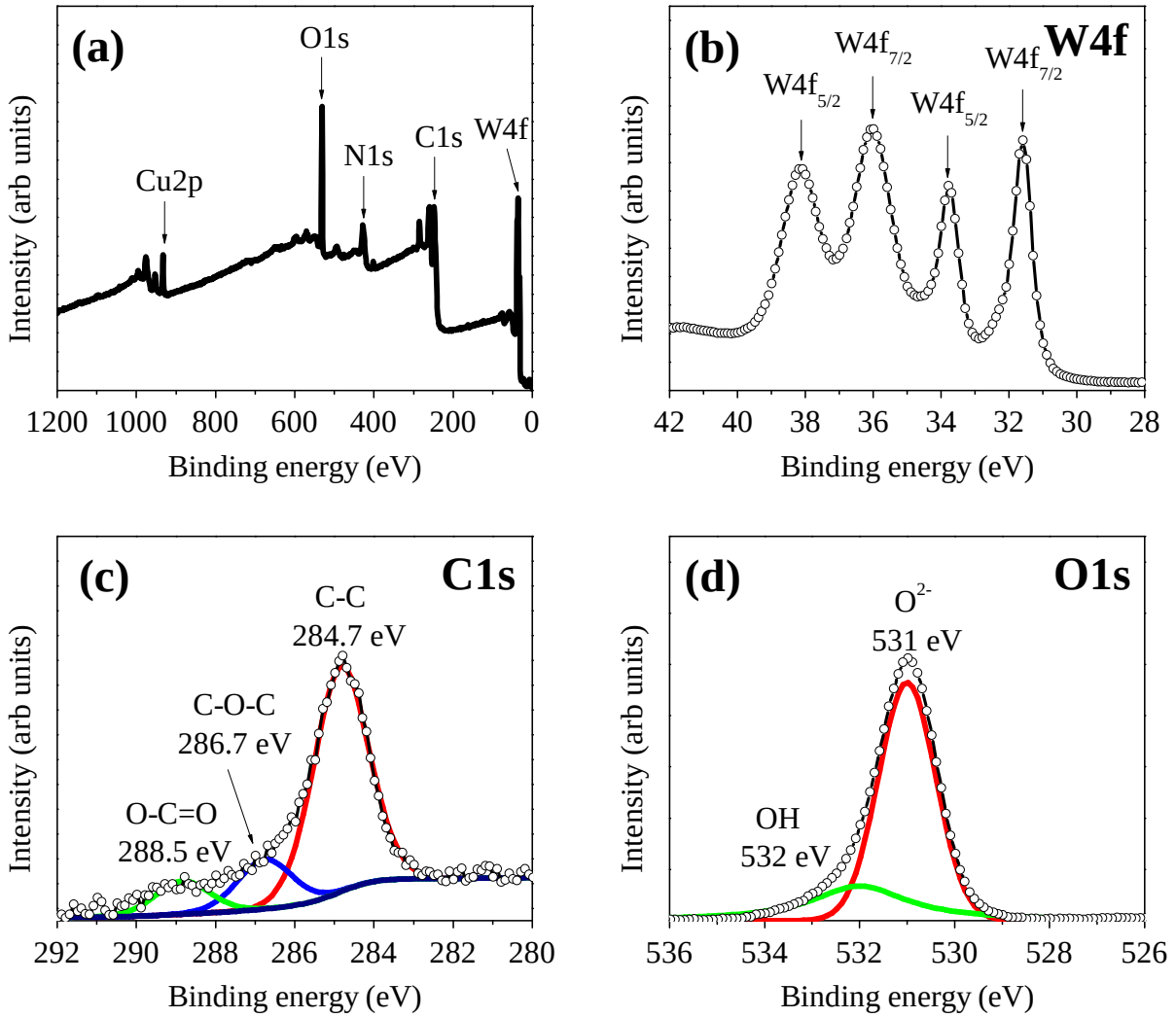

Figure 3.6: XPS core-level spectra of the following regions: (a) long scan, (b)W 4f, (c)C 1s, and (d)O 1s.

The carbon peak, presented in figure 3.6(c), is deconvoluted into three resolved peaks with binding energies 284.7 eV, 286.7 eV, and 288.5 eV. The stronger peak at 284.7 eV is assigned to C−C bonds [83]; while low intensity peaks located at 286.7 eV and 288.5 eV are assigned to C−O−C and O−C=O, respectively [84–88].

On the regard of oxygen, the deconvolution peaks are presented in figure 3.6(d). Peaks are located at 531.0 eV and 532.0 eV. The main peak – 531 eV – is attributed to 1s oxygen ions in the O^{2-} lattice combined with W ions [89–91]. In comparison, the peak located at 532 eV is related to OH^{-} compounds in which there are weakly absorbed oxygen states, or surface contamination [89, 90, 92]. Such contamination is explained by the fact that the device was not characterized in-situ. As a consequence, metallic W was spontaneously oxidized when exposed to atmosphere. In fact, the presence of C−O bonds is also another contamination source, which takes place upon exposing samples to air [92]. More specifically about carbon on the thin film synthesized, similar to oxygen a thin layer, known as adventious carbon, can be found in samples exposed to air. This layer is

composed of relatively short chains, and hydrocarbon species [56]. Additionally, in vacuum systems oil arising from the pump can be a carbon source, with the carbon coat present on tungsten filament, as well as CO and CO_2 species adsorbed in the XPS chamber [56,93–95]. This adventitious carbon is in fact a molecule of interest, once according to literature carbon brings stability to supercapacitors.

3.5.5 Electrochemical studies

Cyclic voltammetry findings are presented in figures 3.8(a-b) and 3.7(a-b). All experiments were performed using W_2C:W_xO_y electrodes separated by a mesoporous membrane soaked with the 1 mol/l Li_2SO_4 and 0.5 mol/l Na_2SO_4 solutions. The molarities informed were picked out from the literature in order to permit carrying out thousand of charge/discharge cycles for pristine carbon allotrope electrodes [35,96].

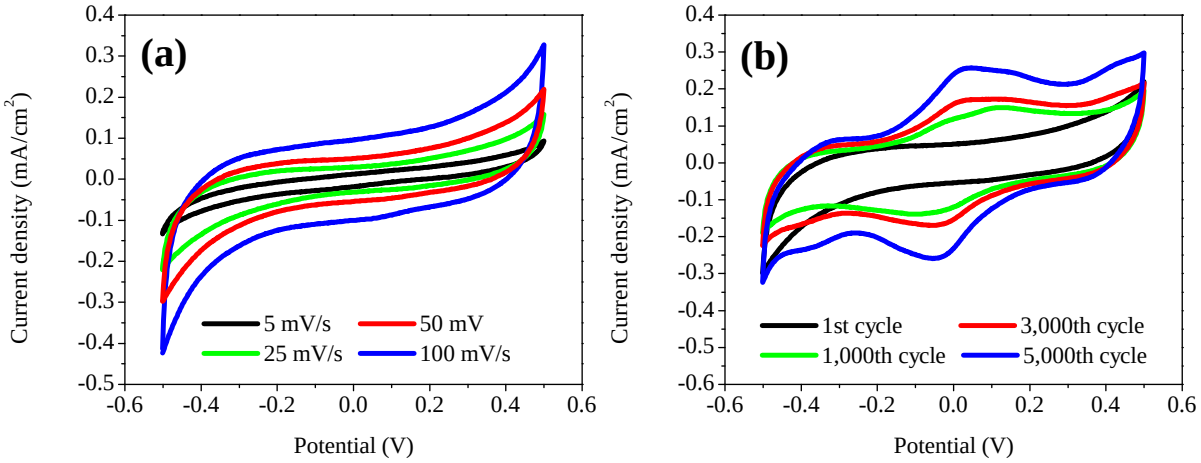

Figure 3.7: (a) Cyclic voltammetry for different scan rates for 0.5 mol/l Na_2SO_4 electrolyte before starting GCD. (b) Cyclic Voltammograms of W_2C:W_xO_y composite electrodes at scan rate 50 mV/s

.

Figures 3.8(a) and 3.7(a) show that as the scan rate increases, the shape of the voltammograms hardly changes, evidencing good electrochemical reversibility as well as high power performance [80]. Also, current is almost a linear function with the scan rate.

In addition, it is possible to observe that as the device is subjected to the GCD cycles it presented clearly distinctive cathodic and anodic peaks, both assigned to pseudocapacitive behavior. Furthermore, according to the voltammograms obtained for the different electrolytes, it is possible to observe one relevant aspect of the electrode: a capacitance increasing over time due to Faradaic reactions, which become evident on the oxidation and reduction peaks present on CV (please see figure 3.8(a) and 3.7(a)).

In fact, there are few peaks and bands appearing on CV. We believe that the redox peaks are due to oxidation and reduction of $W^{6+} \rightleftharpoons W^{5+}$, and also intercalation and deintercalation, according to the relation 3.1 [97,98].

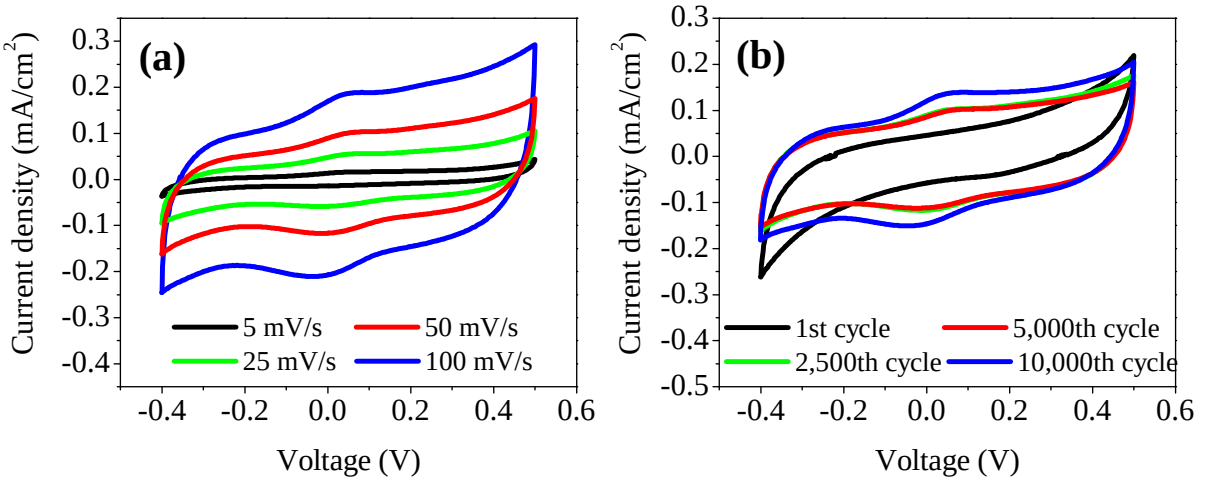

Figure 3.8: (a) Cyclic voltammetry for different scan rates for 1 mol/l Li_2SO_4 electrolyte after 2500 cycles of GCD. (b) Cyclic voltammograms of W_2C:W_xO_y composite electrodes at scan rate 50 mV/s.

$$WO_3 + x\,e^- + x\,M^+ \rightleftharpoons M_xWO_3 \tag{3.1}$$

Where, in reaction 3.1, M^+ can be either Li^+ or Na^+, cations from electrolyte [98].

It is also important to highlight that there is not only WO_3 as tungsten oxide species in the sample, but W_xO_y species, for instance, probably $WO_{2.75}$. Consequently, for both electrolytes studied, the linear increasing in the potential shows two anodic current peaks at approximately 0.1 V and 0.5 V regardless the electrolyte. This happens probably due to oxidation of metallic tungsten and/or W_2C into W_xO_y species [99].

In contrast, driving the voltage to negative values accounts for the reduction of W_xO_y species. This is a relevant fact once publications claim that the decrease in the capacitance is usually because such reduction process generates not W_2C but atomic tungsten and oxygen. Subsequently, after a complete voltammetric cycle, these elements generate inert oxide species on the surface, reducing the accessible W_2C. This oxide, then, provides lower oxidation current values in the subsequent cycles; therefore, decreasing the capacitance [99].

Nonetheless, this fact is not applicable to the present study – opposite to what was found out by several publications – once there is capacitance increase after GCD cycles [100]. Figure 3.9 illustrates such capacitance enhancement.

Another hypothesis that justifies such capacitance increase is the H^+ storage within the WO_3 crystal structure [101]. This process obeys the following reaction.

$$WO_3 + x\,H^+ + x\,e^- \rightleftharpoons H_xWO_3 \tag{3.2}$$

Although H^+ – proton – insertion/extraction is an important topic for electrochemical performance, to date, such mechanism is not thorough understood for lattice

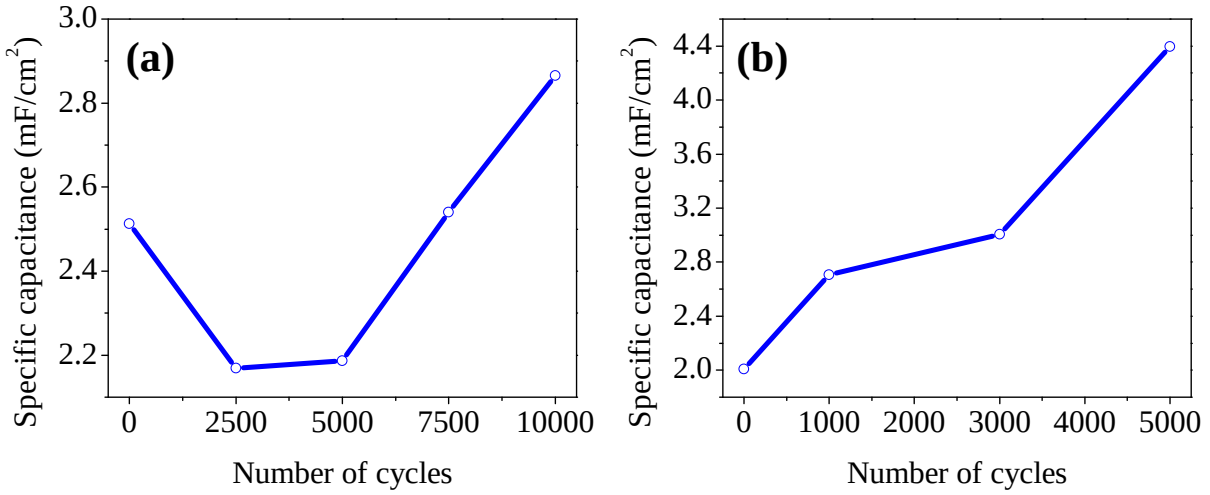

Figure 3.9: Specific capacitance for W_2C:W_xO_y composite devices with (a) 1 mol/l of Li_2SO_4 and (b) 0.5 mol/l of Na_2SO_4.

water in WO_3 [101]. Orisini *et al* reported that mesoporous WO_3 in aqueous media combines good proton and electron conduction, consolidating a mixed conductive system [102]. According to these authors, pore surface with charged defects promotes dissociation of protons from the chemisorbed water. In this study there is some further analysis aiming to elucidate the electrochemical behavior of the supercapacitor device.

A detailed analysis of capacitance – illustrated in figure 3.9 – shows that for 1 mol/l of Li_2SO_4 there is an increase of approximately 14% in the capacitance, from the very first cycle up to $10,000^{\text{th}}$ cycle. Similarly, for 0.5 mol/l of Na_2SO_4, there is an increase of 119% from the very first cycle up to $5,000^{\text{th}}$ cycle, as showed by figure 3.9(a-b). These results are also discussed in more details below.

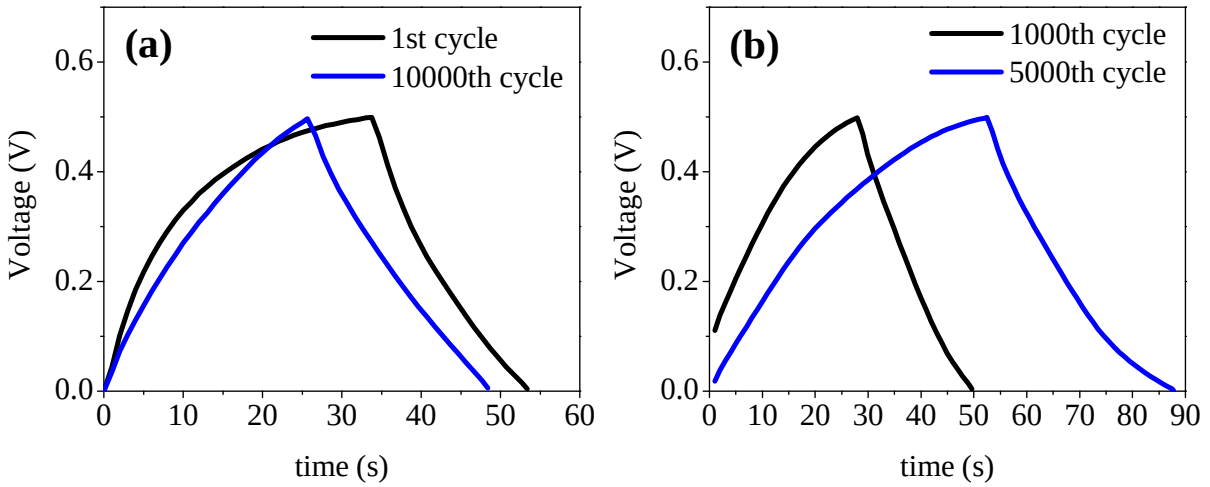

Figure 3.10: Galvanostatic charge-discharge for W_2C:W_xO_y composite devices with (a) 1 mol/l of Li_2SO_4 electrolyte from 1^{st} and $10,000^{\text{th}}$ cycles, and (b) 0.5 mol/l of Na_2SO_4 from $1,000^{\text{th}}$ and $5,000^{\text{th}}$ cycles.

Another important aspect regarding the characterization of supercapacitors is the

efficiency, which is calculated by inserting variables extracted from GCD figure 3.10(a-b) onto equation 2.20.

For the electrochemical capacitor with 1 mol/l of Li_2SO_4, at 1^{st} cycle the calculated efficiency is 59%; while, in $10,000^{th}$ cycle it is 89%. Accordingly, efficiency increased 50.8% over time for that device. On the other hand, for supercapacitor with 0.5 mol/l of Na_2SO_4, in the $1,000^{th}$ cycle, the efficiency is 78%; whilst in $5,000^{th}$ cycle it is 67%. Hence, a variation of -14.1% over time. With respect to this efficiency decrease – as showed in figure 3.10(b) – the wider voltage window of the device with 0.5 mol/l of Na_2SO_4 has probably interference in this aspect.

As previously stated, further elucidation of the processes occurring in the electrolyte and at the electrode/electrolyte interface were investigated using the EIS technique. Figures 3.11 and 3.12 show EIS spectra registered using the Li_2SO_4 and Na_2SO_4 electrolytes, respectively. Values of the circuit elements in figure 2.9 were extracted and presented in tables 3.1 and 3.2.

R_{esr} (equivalent series resistance) values are presented in table 3.1. R_{esr} stands for sum of the thin-film resistance, overall impedance of the current collector, void resistance in the electrode micro-structure, and electrolyte resistance [2]. In addition, in the case of the constant-phase element (CPE) used to represent the non-ideal capacitive behavior of solid electrodes, one has the parameter denoted as Y_0 – depicted in table 3.1 – which represents the non-ideal capacitance values (e.g., fractal behavior) denoted by $C_{PE_{EDL}}$ and C_{PE_θ}. Accordingly, EIS analysis also shows capacitance increase; thus, corroborating with the experimental findings obtained for the Li_2SO_4 electrolyte from cyclic voltammetry and GCD techniques.

Table 3.1: Data extracted from EIS for the device with 1 mol/l of Li_2SO_4.

Cycles	R_{esr} (Ω)	R_{ct} (mΩ)	$C_{PE_{EDL}} - Y_0$		$C_{PE_\theta} - Y_0$	
			n	$[(m\Omega^{-1} * s)^n]$	n	$[(m\Omega^{-1} * s)^n]$
2500	4.42	415	0.771	0.876	0.777	2.21
10000	4.14	707	0.783	1.07	0.754	2.52

Regarding the capacitance enhancement, this capability is achieved possibly due to greater accessibility of electrode surface to the electrolyte ions during GCD. It means that the material synthesized at the present study is capable of providing better access to pores on its surface; thus, outperforming previous studies [48, 50, 54]. We believe the capacitance of the device containing Na_2SO_4 electrolyte becomes more pronounced because of the size of hydrated Na^+ ions is 3.59 Å. On the contrary, in the case of the bulky Li^+ ions, one has a value of 3.81 Å. Thus, Na^+ ions might exhibit better access to narrower

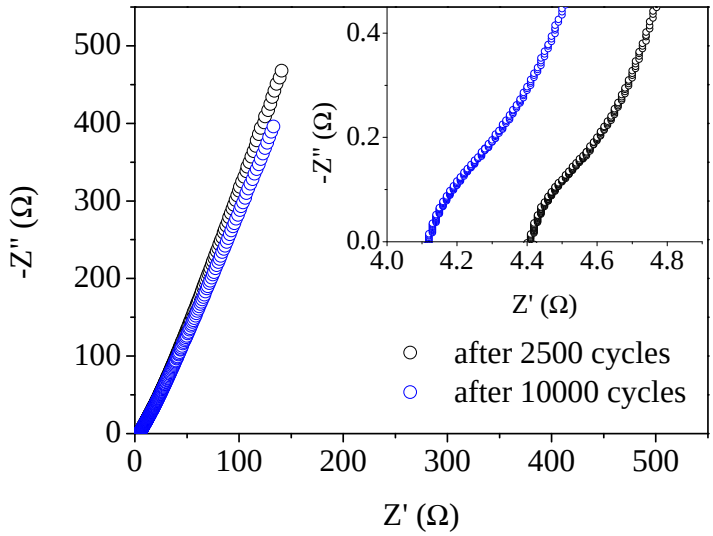

Figure 3.11: EIS for 2,500th and 10,000th cycles for Li_2SO_4 electrolyte.

pores of the composite surface [103]. Indeed, more accessible active sites means more energy stored.

Furthermore, according to table 3.2, R_{esr} increased over time approximately 50.5%, which indicates formation of a passive layer. Regarding the R_{ct} (charge transfer resistance), according to table 3.2, it increased over time, also probably due to larger covering and thicker oxide layer formation which limits the electron transfer at the electrode/electrolyte interface.

Table 3.2: EIS data for EC filled with Na_2SO_4 electrolyte after 2500th and 10000th cycles.

Cycles	R_{esr} (Ω)	R_{ct} (mΩ)	$C_{PE_{EDL}} - Y_0$		$C_{PE_\theta} - Y_0$	
			n	$[(m\Omega^{-1} * s)^n]$	n	$[(m\Omega^{-1} * s)^n]$
1st	1.01	276	0.997	0.896	0.847	1.99
5000	1.52	299	0.816	1.93	0.81	2.45

Similarly to the supercapacitor with 1 mol/l of Li_2SO_4, the capacitance obtained in 0.5 mol/l of Na_2SO_4 increased considerably, as presented in figure 3.7(b). The explanation for that probably lies on the occurrence of an activated transport process, which means the electrolyte gradually penetrates in the surface pores facilitating the ion insertion/extraction process. As a result, one has the occurrence of facilitated redox reactions throughout the electrode surface [54, 80]. This feature is corroborated by the values of Y_0 – $C_{PE_{EDL}}$ and C_{PE_θ} – columns in table 3.2.

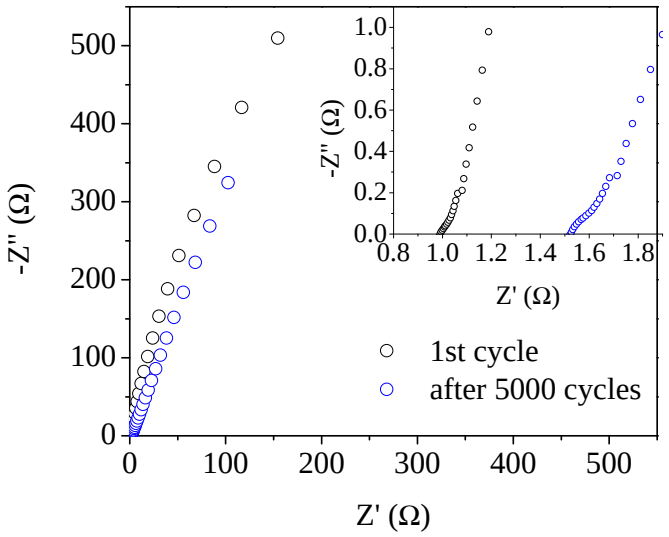

Figure 3.12: EIS data from EC filled with Na_2SO_4 electrolyte after first and 5,000th cycles.

3.6 Conclusions

This work presents the growth of W_2C:W_xO_y thin film using the HFCVD method. The method employed aimed at obtaining a material with a Faradaic behavior – due to oxidation and reduction processes – without jeopardizing the thin-film electrical conductivity properties. For this purpose, spontaneous passivation was the technique chosen to form the oxide layer on the W_2C:W_xO_y thin film. The electrochemical results showed that supercapacitors, tested with 1 mol/l Li_2SO_4 and 0.5 mol/l Na_2SO_4 electrolytes, withstood more than 5,000 cycles each, increasing its capacitance during the tests. Enhancement on the electric properties of the device is probably caused by activation of the nanometric oxide layer promoted during the GCD experiments. Only few studies that employed WO_3 have reported any enhancement of the device capacitance. In fact, most of them have reported a considerable decrease in capacitance values after few hundred cycles. Indeed, the ion insertion/extraction during Faradaic reactions can be responsible for the capacitance increase, once more pores are available and therefore the electrolyte can easier access them for faster exchange of electrons and protons all over the accessible surface regions. It is evident that with R_{esr} decrease – for Li_2SO_4 electrolyte device – the electrode wettability increases; therefore, facilitating the ion permeability and decreasing the "void regions" formed by gases captured from the environment during the device assembling process. Therefore, results obtained in the present work, for both electrolytes, contribute to the development of electronic devices, such as wearables that self-improve its electric characteristics during use, once the cycling tests simulate real conditions of operation. Additionally, it is worth noting that other devices can be powered by this supercapacitor; by associating supercapacitors other applications may also use this environmentally friendly energy storage device.

Chapter 4

Core/shell Nb_2O_5 nanoparticles/carbon on carbon nanotubes as symmetrical supercapacitor electrodes

4.1 Introduction

Niobium composites started to gain attention in the last decades due to its applications for industry, in particular at aerospace sector – owing to super alloys – and electro-electronic [104]. Furthermore, niobium is recognized as critical raw material for European Union and American industries. In this regard, Brazil is a privileged country, once it holds more than 90% of world's exploitable niobium reserves [105].

In the regard of supercapacitors, as previously stated at present study, transition metal oxides are species of interest due to pseudocapacitive behavior they may present [7]. Examples of transition metal oxides widely reported in literature for supercapacitors are: RuO_2, NiO, Co_3O_4, $NiCo_2O_4$, TiO_2, Fe_2O_3, and Nb_2O_5 [106].

One of the most known niobium compounds, niobium pentoxide (Nb_2O_5), is a n-type semiconductor – band gap of 3.4 eV – important due to its technological applications. It is a material of interest owing to its chemical and physical properties. Some of its applications are biomaterials, gas sensors, optical filters, catalysis, solar cells, and electronics [107]. In addition, Nb_2O_5 is a promising candidate for energy storage applications due to its pseudocapacitance and high power and energy features [108–111]. Factors that contribute to its employability are the low cost, high chemical stability, environment-friendly, redox valence states, wide range of temperatures and high potential window [106, 112–114].

Even though this material has interesting properties, publications that present Nb_2O_5 nanocomposite materials for energy storage electrodes are considered rare [110]. One reason for that lies in the fact that niobium species started to gain attention in the 90s, mainly in heterogeneous catalysis research field, thanks to publications which reported

that the addition of niobium could increase the catalytic activity, selectivity and chemical stability of traditional catalysts. Thus, ever since interest in niobium has increased, as well as in its oxides, either as active phase or support [105].

It is also important to highlight that Nb_2O_5 is polymorph, which means it presents several crystal structures, namely: pseudo-hexagonal, orthorhombic, tetragonal, and monoclinic [115]. Monoclinic, tetragonal and orthorhombic phases are reported as suitable for applications in energy conversion and storage. [109, 116] Monoclinic is the most stable phase thermodynamically; whilst pseudo-hexagonal is the least [109].

Moreover, when it comes to supercapacitors, regardless of the surface area, Nb_2O_5 orthorhombic phase has presented the highest specific capacitance, when compared to the other phases and to RuO_2 – transition metal oxide with the highest specific capacitance known [9, 117, 118]. Figure 4.1 presents the crystal structure and the relation with calcination temperature.

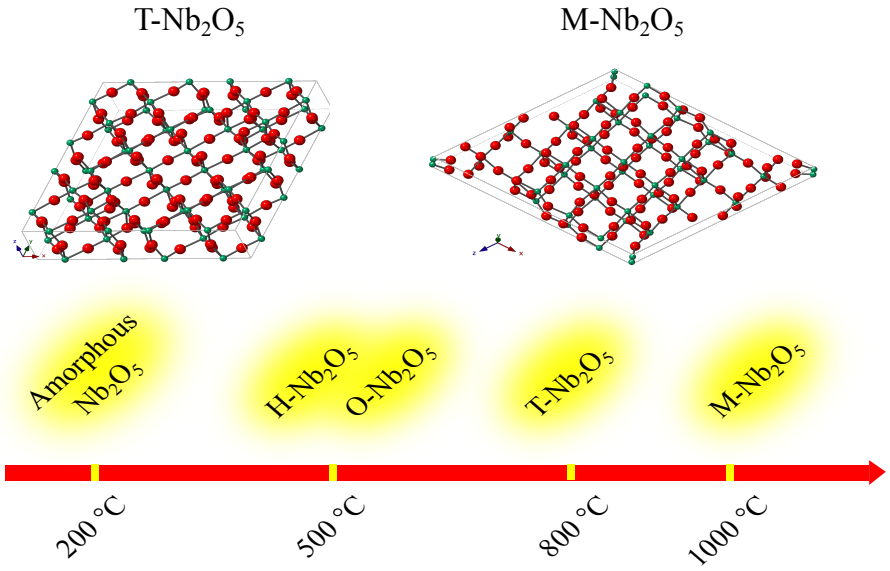

Figure 4.1: Structural representations of some crystal structures of Nb_2O_5 with their respective phase in function of temperature. Adapted from [9]

.

Nevertheless, the drawback of employing Nb_2O_5 in supercapacitors lies on its low electric conductivity – $\sigma \approx 3.4 \times 10^{-6}\,\mathrm{S/cm}$ – and easy passivation [110, 119]. Aiming to overcome such drawbacks, a technique for decoration was employed as the amount of Nb_2O_5 should be the necessary to provide pseudocapacitive behavior but without jeopardizing the electronic conductivity of the thin film. To that end, a technique known as electrospray was chosen towards decoration with Nb_2O_5 for this study.

The electrospray method aims at ionization of particles by applying a high electric field. The droplets are then charged to a fraction of the Rayleigh limit, which is the droplet electric charge magnitude that overcomes its surface tension force, leading, then, to its fission [10]. Such fission generates droplets extremely small, down to nanometers, as

well as elongation of the jet – process known as Taylor cone – caused by the electric field action in the shear stress of the liquid surface. In addition, the droplets tend to split until they reach the gaseous phase. By charging the particles with same polarity, they are apart thanks to Van der Waals forces [120].

Therefore, at this study we combined strategies aiming to employ innovative, low-cost and clean techniques in order to come up with an feasible stable current collector with enhanced conductivity, chemical stability, avoiding agglomeration of niobium pentoxide particles. Also, it is reported by literature that nanometric metal oxide crystals present greater pseudocapacitive responses, owing to higher density of active surface as well as short pathways [121].

First, we worked with niobium pentoxide nanoparticles, which have high concentration of dangling bond per unit of volume compared to bulk material. Furthermore, they present shorter diffusion length and the larger electrode-electrolyte interface area compared with the bulk structure [117]. Second, we partially covered niobium pentoxides nanoparticles with thin carbonaceous layer with the goal to enhance electronic conductivity (e.g. kinetics enhancement of electrode material) and avoid aggregation of Nb_2O_5 nanoparticles. We employed Ni_xAl and MWCNT as current collector to fast and efficiently drain electrons from Nb_2O_5 nanoparticles. This coating technique – with of high voltage deagglomeration – of Nb_2O_5 consolidated a novel composite material which we henceforth refer as $Ni_xAl : MWCNT - Nb_2O_5$. Ni_xAl is a modified aluminum foil, which is converted into nickel and aluminum alloy, showing metallic electrical conductivity with chemical stability on aqueous media [35]. Thus, $Ni_xAl : MWCNT - Nb_2O_5$ has superior electrochemical properties, including longer lifespan along with higher energy and power densities, because of the synergistic effects of the Ni_xAl current collector, mesoporous carbon and pseudocapacitive properties from Nb_2O_5.

More importantly, the EC assembled were symmetrical. To our best knowledge, no work has been published on symmetrical supercapacitors with Nb_2O_5/MWCNT electrodes operating in high voltage in aqueous electrolytes.

Regarding electrolytes, aqueous ones are unique due to its environment-friendly, high ionic conductivity, low cost, and easy manufacturing and handling characteristics. It is worth noting, nevertheless, that they posses limitations in its voltage compared to organic solvents and ionic electrolytes. Such limitation happens due to H_2/O_2 evolution reactions – at 1 atm and room temperature – for voltages higher than 1.23 V [38]. In contrast, at present work the supercapacitor operated at 1.8 V for almost 200,000 cycles; hence, another relevant aspect of this study.

Thus, for the reasons presented herein, Nb_2O_5 is a promising candidate for supercapacitors electrodes. Its poor electric conductivity can be overcame by calcination under high temperature [113].

4.2 Experimental procedures

In order to prepare the current collectors, aluminum foil substrates were cut in squares with dimensions of 3 cm by 3 cm and treated in a solution containing hydrochloric acid (HCl) and deionized water (1:4) for 30 s. The samples were then transfered to an electrodeposition system, where at 60 °C a current density of 25 mA/cm^2 circulated for 1 min in a solution containing 2 mol/l $Ni(NO_3)_2$. In this process, a layer of Ni was formed and because of the heat it was transformed into catalyst spheres, which are encapsulated by CNT.

After properly dried, samples were placed inside chemical vapor deposition (CVD) furnace for MWCNT growth. After purging the system with N_2, temperature was increased up to 650 °C. After temperature stabilized for 5 min, carbon feedstock containing 43.6 wt% of camphor ($C_{10}H_{16}O$) diluted in ethanol (C_2H_5OH) with 2 wt% of $Ni(NO_3)_2$ was released into the furnace by N_2 drag for 60 min.

Once the samples were cooled down to room temperature, the electrospray ionization procedure was performed in order to equally distribute Nb_2O_5 nanoparticles onto MWCNT surface. In this process, Nb_2O_5 optical grade – which present the best optical transmission and was kindly donated by Brazilian metallurgy and mining company (CBMM) – was deposited onto the MWCNT samples as grew by a technique known as electrospray [122].

For this deposition, which configuration is portrayed by figure 4.2, the positive terminal of a direct current (DC) high voltage source is connected to one syringe needle; while the substrate is grounded. The voltage applied to the syringe capillary was 10 kV for 1 s, and the mixture in the syringe contained 0.05 mol/l of Nb_2O_5 in methanol. It is worth mentioning that such molarity was found in literature and experimentally, once the Nb_2O_5 is an insulating composite [9]. This means that higher concentrations of Nb_2O_5 probably would give to the CNT grew an insulating nature; therefore, hindering its capacitive performance.

Afterwards, calcination process was performed aiming to provide the desired crystal structure. Furthermore, in calcination it is possible to convert the insulating Nb_2O_5 particles into conductive NbO and NbO_2 by phase transformation and by increasing the carbon content on the electrode, aspect that may improve the electrochemical performance, once it may provide maximum access of pores to aqueous electrolyte species [123]. In contrast, the surface area can be reduced in calcination process [9]. This process was also performed in CVD furnace under constant flow of 1×10^3 sccm of N_2 for 1 h and 650 °C. Overall, the experimental results show that calcination process should be performed right after electrospray ionization (ESI) process. As a matter of fact, all reagents used in this experiment were guaranteed-grade and used without further purification.

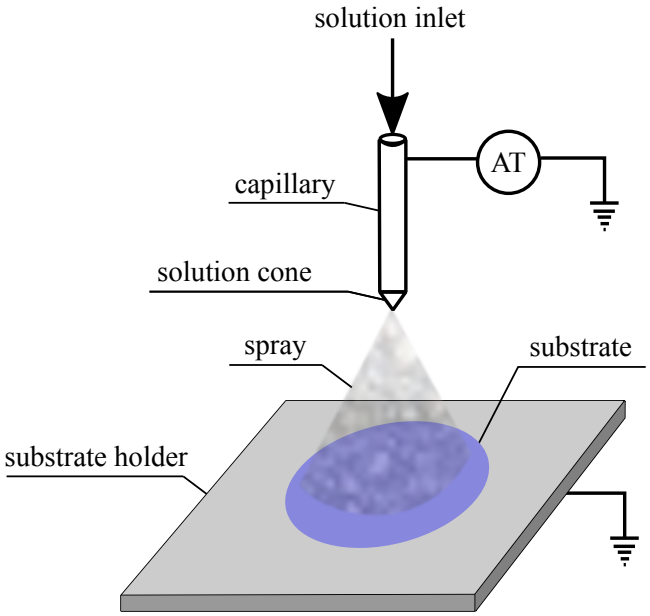

Figure 4.2: Simple nozzle configuration for electrospray system. Adapted from [10].

4.3 Materials characterization

In relation to characterizations at this study, for the morphology of the thin films grew, scanning electron microscope (SEM) and transmission electron microscopy (TEM) were performed, respectively, by FEI Quanta 650 FEG and JEOL 2100 MSC. Additionally, the technique essential for carbonaceous materials evaluation – Raman spectroscopy – was performed by Renishaw inVia with laser Ar^+ of 2.41 eV (514.5 nm). XPS spectrum was taken by Thermo K-α XPS, monochromatic small-spot, Al anode, (hν = 1486 eV), spot 400 μm.

4.4 Devices characterization

Electrochemical characterization was performed by Ametek Versa STAT 4 potentiostat-galvanostat in two-electrode system, assembled in a 2032-coin cell-type, as presented in figure 3.2. All experiments were performed using $Ni_xAl : MWCNT - Nb_2O_5$ composite as electrodes separated by mesoporous membrane, all wet by 1 mol/l Li_2SO_4. Cyclic voltammetry (CV) was performed from 0.01 to 1 V/s; galvanostatic charge discharge (GCD) was carried out from 5.8 to 176 A/g; and electrochemical impedance spectroscopy (EIS) was performed at 500 mV with amplitude of 10 mV from 0.10 Hz up to 10 kHz.

4.5 Results and discussion

4.5.1 Morphology

Firstly, figure 4.3(a-f) shows that Nb_2O_5 particles were distributed all over CNT surface. Therefore, due to the magnification depicted, there are nano-size Nb_2O_5 particles deposited on the carbonaceous thin film grew from CVD process.

Furthermore, ESI plays an important role on Nb_2O_5 deagglomeration and distribution on the CNT surface. Figure 4.3(e-f) illustrates the high density of CNT decorated with quasi-spherical small nanoparticles – possessing 100 nm or less. Also, figure 4.3(g-l) depicts TEM images, evidencing turbostratic MWCNT encapsulating nickel catalytic particles, which are only very small portion of particles. Regarding the CNT, they possess a few dozen walls with basal planes slipped out of the radial alignment, and with interplanar spacing of 0.32 ± 0.02 nm. CNT diameters range from 20 to 60 nm, which are decorated with niobium oxides nanoparticles with diameters ranging from 10 up to 100 nm. Also, carbon and niobium pentoxide are on crystalline phase with lattice fringes evidenced under appropriate focus. It is clear here that niobium oxides nanoparticles are and inside the core encapsulated for carbon shell, which has few nanometers thickness. MWCNT form an entangled spaghetti-like network; therefore, contributing towards electric conductivity. In order to better understand material properties and electrochemical behavior of this novel material, further characterizations are presented herein.

4.5.2 Raman spectroscopy

According to figure 4.4, Raman mode ν_1 is most diagnostic in niobium oxide materials and corresponds to the symmetric metal-oxygen stretching vibration on octahedral structure [124, 125]. Raman band at $235\,cm^{-1}$ is characteristic of bending mode of Nb–O–Nb, also reported as ν_6 (T_{2u}) mode [125–127], while the band located at $\approx 840\,cm^{-1}$ is assigned to Nb–O–Nb collinear bond symmetric stretching [128]. Furthermore, the bands within range 500-800 cm^{-1} are assigned to Nb–O–Nb symmetric and anti-symmetric stretching modes; while the doubled observed with bands located at ≈ 630 and $680\,cm^{-1}$ are assigned to transverse optic modes (TO) or a less ordered structure, as when the transition happens to T-Nb_2O_5 (orthorhombic), the peak at $675\,cm^{-1}$ shifts to $700\,cm^{-1}$ [127, 129–131]. Finally, the band located at $993\,cm^{-1}$ corresponds to Nb_2O_5 to stretching vibrations of the Nb–O bond. [126, 129, 131]. Thus, crystal structure of Nb_2O_5, it presents a phase transformation from amorphous to pseudo hexagonal [127, 132]. In addition, it also presents monoclinic phase, as well [127].

Regarding the carbon Raman peaks, the band characteristic for quantifying disorder in carbonaceous materials – known as D band – is located at $1350\,cm^{-1}$. The

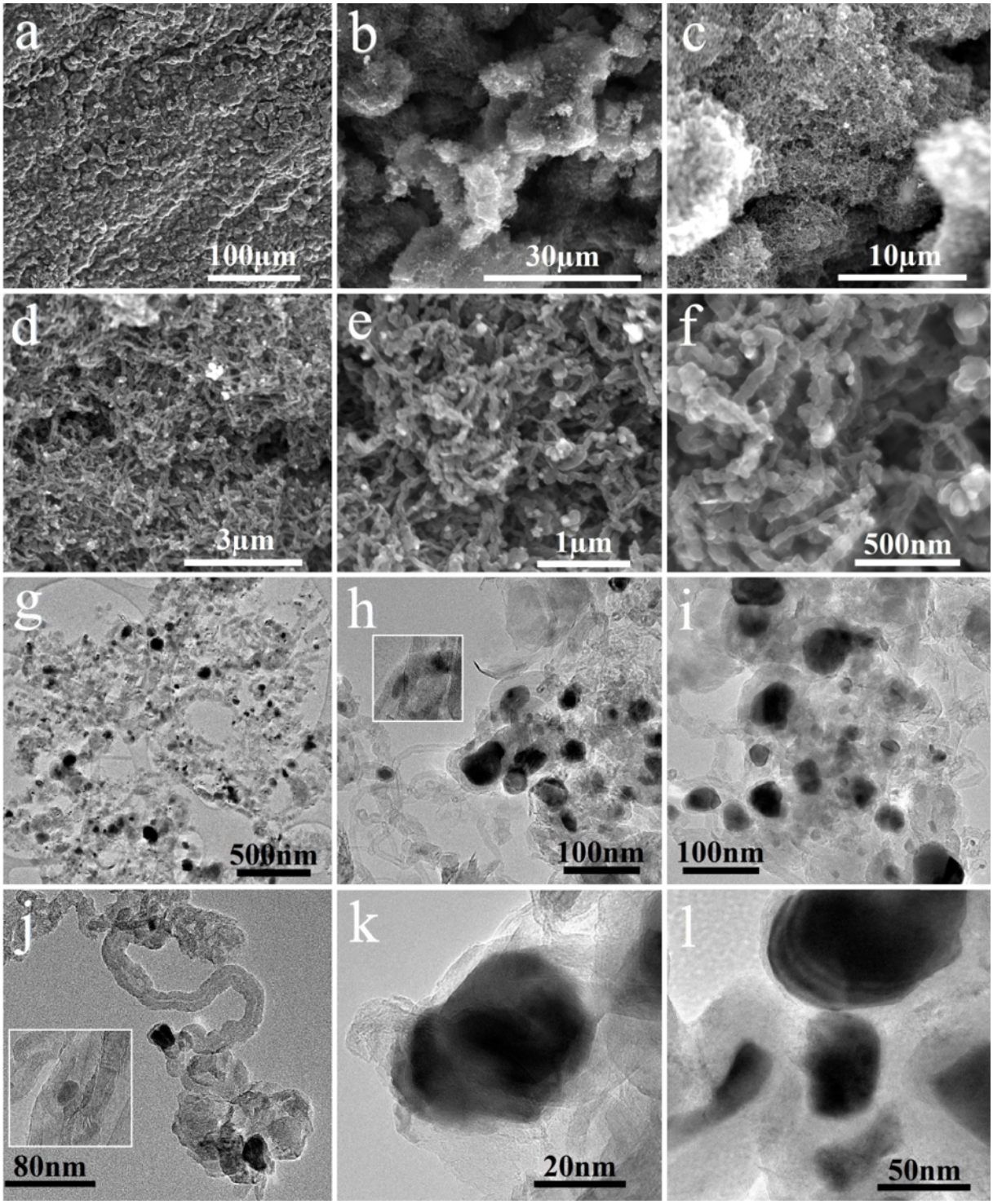

Figure 4.3: SEM and TEM from the MWCNT decorated with Nb_2O_5.

G band – also known as E_{2g} or graphitic carbon – is located at $\approx 1580\,cm^{-1}$; whereas D' peak is at $1620\,cm^{-1}$ [133–135]. Furthermore, according to the Raman spectra, the MWCNTs synthesized are a highly crystalline sp^2 based material full of structural defects. These defects may enhance the adsorption, bonding, mass transport and conductivity.

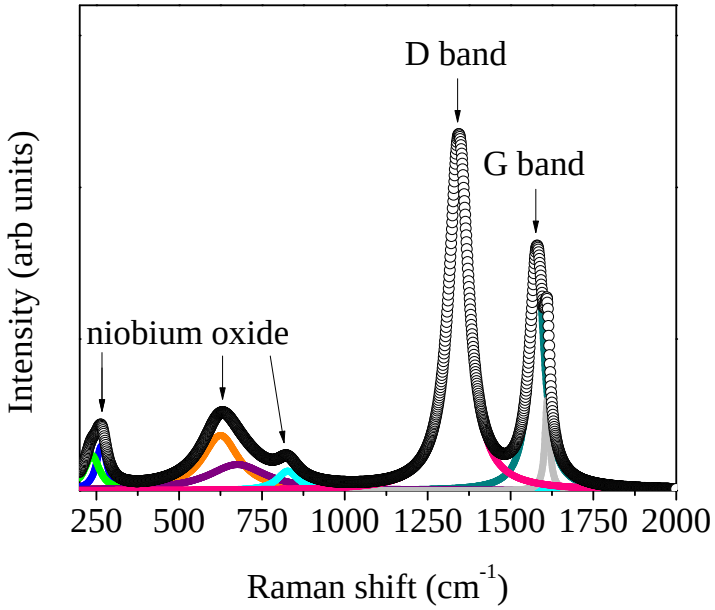

Figure 4.4: Raman spectrum of compound MWCNT decorated with Nb_2O_5.

4.5.3 X-ray photoelectron spectroscopy analysis (XPS)

XPS measurements were performed for further investigation of the material obtained. The deconvoluted curves are presented by figure 4.5(a-f). Importantly, figure 4.5(a) presents the species present in the sample.

About Nb 3d nanocomposite spectrum, one shows that binding energies for Nb $3d_{3/2}$ and $3d_{5/2}$ are 210.6 eV and 207.9 eV, respectively. Additionally, the ionic state is Nb^{5+} and the double-peak structure is 2.7 eV, all results in accordance with published results [110, 121, 136–138].

Regarding O 1s spectrum, according to figure 4.5(c), it presents two peaks. The first one – located at 530.7 eV is assigned to O^{2-}, which corresponds to the ion in the Nb_2O_5 species [138–141]. The second one, located at higher binding energy – 532.1 eV – is assigned to hydroxyl group ($-OH$) absorbed on the MWCNT:Nb_2O_5 thin film [142–144].

In C 1s spectrum, portrayed in figure 4.5(d), there are three component peaks at 284.6, 285.6, and 287.3 eV, which are characteristic of C−C bonds [145–147], C−O [86], and C=O bonds [146], respectively.

For nickel binding energy range, one is presented in figure 4.5(e). It is possible to see the metallic nickel peak at 852.8 eV [148, 149]. Also, there is a Ni $2p_{3/2}$ multiplet-split at $\approx$ 854.7 eV and 856.4 eV, which indicates the presence of NiO on the surface, probably due to passivation occurred after electrodeposition procedure [150–155]. Furthermore, from the binding energies presented, the oxidation state of NiO is Ni^{2+} and the peak located at 854.7 eV is due to a satellite peak of Ni $2p_{3/2}$ located at 861.6 eV [149, 152, 154, 156]. Other small intensity peaks depicted on figure 4.5(e) were assigned as Ni $2p_{3/2}$ satellites, more specifically the ones located at 858.8 eV, 862.8 eV and 864.9 eV [155, 157, 158].

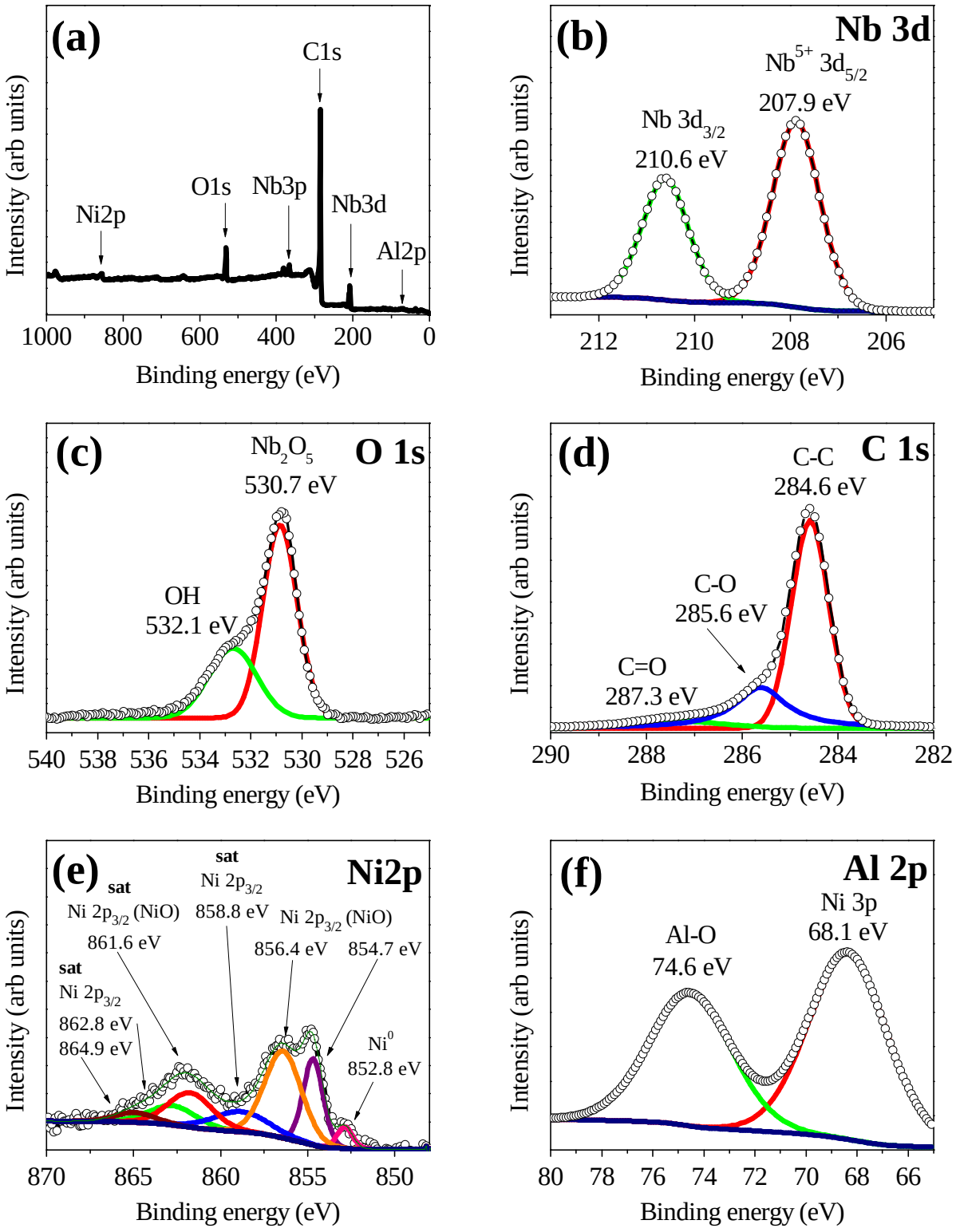

Figure 4.5: XPS core-level spectra of the following sections: (a) long scan, (b)Nb 3d, (c)O 1s, (d)C 1s, (e)Ni 2p, and (f)Al 2p.

Finally, as presented in figure 4.5(f), Al 2p band at 74.7 eV is assigned to Al−O species, probably Al_2O_3 generated due to passivation of the substrate; while the signal at 68.1 eV is assigned to Ni 3p, which formed a metallic alloy with aluminum [151, 159, 160].

4.5.4 Electrochemical studies

According to literature, pristine MWCNT electrodes present capacitance ranging from 4-135 F/g [161]. Figure 4.6(a) shows specific capacitance comparison of a pristine MWCNT and Ni_x : Al:MWCNT-Nb_2O_5 electrodes, both tested in 1 mol/l Li_2SO_4. From this data, it is evident the superiority of Ni_x : Al:MWCNT-Nb_2O_5 composite, which presents specific capacitance – operating at 1.8 V – of 464.7 F/g; whilst the pristine MWCNT depicted presents specific capacitance of 13.6 F/g. Therefore, by employing the ESI decoration with Nb_2O_5, the capacitance was increased more than 34 times.

Another relevant aspect of the as-grew composite is the high operating voltage – 1.8 V – which culminates in greater energy densities, as well as the box-like shape of the voltammogram presented by figure 4.6(b). Such characteristic implies good wettability even under under operation in higher electric potential.

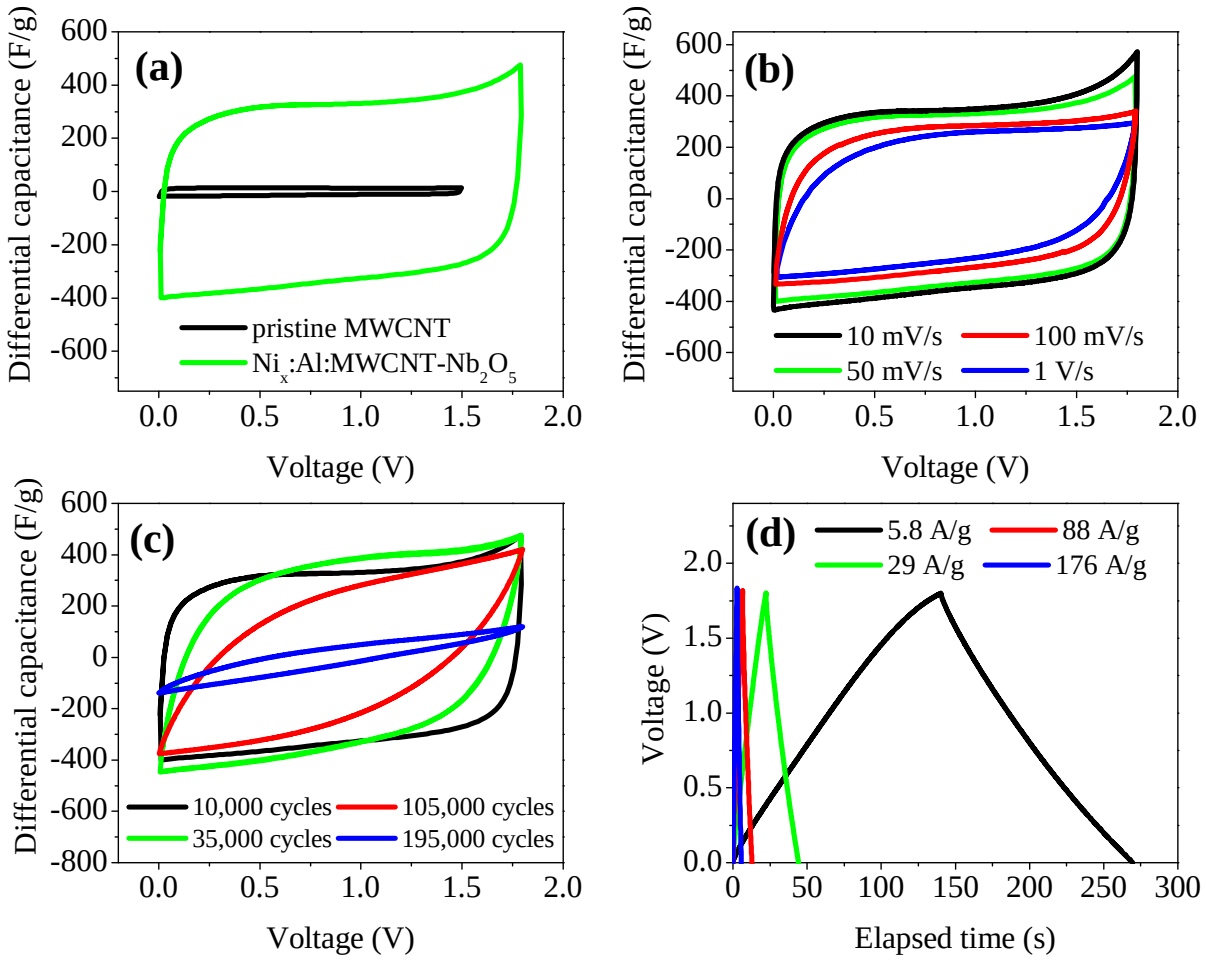

Figure 4.6: (a) Comparison of MWCNT and decorated Nb_2O_5:MWCNT, (b) cyclic voltammetry of Ni_x : Al:MWCNT-Nb_2O_5 electrode for different scan rates, (c) evidences long lifespan of the device and its behavior at 100 mV/s, and (d) galvanostatic charge–discharge (GCD) profiles for various current densities.

Regarding the capacitance enhancement shown by figure 4.6(a), probably the

Nb_2O_5 plays the role towards pseudocapacitance behavior. Although not as evident as the W_2C composite electrode redox peaks, it is possible to see subtle redox peaks in figure 4.6(b). Furthermore, the nanostructured Ni_x : Al:MWCNT-Nb_2O_5 composite with high conductivity – due to carbon shell – may also contribute for pseudocapacitive properties by enabling faster electron transport and rate capability.

It is also important to highlight the long lifespan of the device. Figure 4.6(c) presents CVs after 10,000, 35,0000, 105,000, and 195,000 GCD cycles. From these CV, one can evaluate the big picture regarding impedance, capacitive and pseudocapacitance behavior during GCD cycles, which shows good response even after several GCD cycles. Importantly, the device withstood nearly 200,000 cycles, value greater than usually reported by literature [162–164].

Additionally, EIS was performed aiming to further understand changes in capacitance and resistance of the device. Figure 4.7(a) reports EIS spectra of the device after $10,000^{\text{th}}$ and $105,000^{\text{th}}$ GCD cycles. From such plot, the higher frequency region intercepts the x-axis – real part of impedance – at $\approx 1.28\,\Omega$, which is equivalent to $\approx 2.6\,\text{m}\Omega\,\text{g}$. Thus, it implies at the beginning of GCD in low equivalent series resistance of Ni_x : Al:MWCNT-Nb_2O_5 thin film, probably due to the thin carbon shell around Nb_2O_5 nanoparticles. Likewise, it is worth noting that such carbon shell also contributes towards electrochemical stability, as a protection layer is formed, which provides path for electrons to Nb_2O_5 surface sites [165, 166].

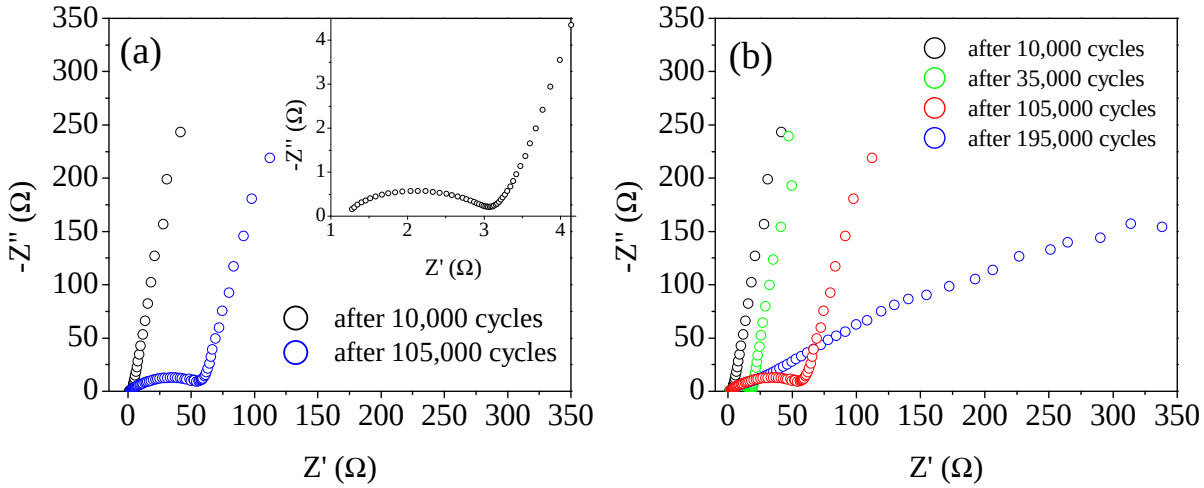

Figure 4.7: (a) EIS data took from device after 12,993rd and 107,886th cycles for Li_2SO_4 electrolyte, and (b) EIS from 12,993rd up to 197,886th cycles for 1 mol/l of Li_2SO_4 electrolyte, showing behavior change of the device as it underwent GCD cycles.

Correspondingly, EIS presented by figure 4.7(b) corroborates the behavior of voltammogram – figure 4.6(c). This data is also in accordance with Randles equivalent circuit – shown by figure 2.9 – whose fitting is detailed in table 4.1. To summarize, at the beginning, the composite presents smaller charge transfer resistance (R_{ct}), as confirmed

by voltammogram, Randles equivalent circuit fitting, and EIS Nyquist plot depicted in figure 4.7(b). As it underwent thousand of GCD cycles, such resistance increased; thus, modifying the semicircle and therefore the values of R_{ct} in table 4.1.

Table 4.1: Data extracted from EIS constant-phase element (CPE).

Cycles	R_{esr} (Ω)	R_{ct} (mΩ)	$C_{PE_{EDL}} - Y_0$		$C_{PE_\theta} - Y_0$	
			n	$[(m\Omega^{-1} * s)^n]$	n	$[(m\Omega^{-1} * s)^n]$
12,993	1.07	2.20	0.608	0.792	0.904	51.3
37,866	1.47	18.6	0.605	0.886	0.934	54.2
107,886	0.905	67.8	0.457	1.79	0.921	52.2

4.6 Conclusions

This study presents the synthesis of a composite named Ni_x : Al:MWCNT-Nb_2O_5 through a facile method. Aiming to come up with an electrode with high electronic conductivity and chemical stability, MWCNT was firstly grew onto the substrate, following the deposition by ESI technique of Nb_2O_5. After this deposition, calcination was performed, which provided the structure named as carbon shell. This structure – carbon shell which wrapped Nb_2O_5 nanoparticles – provided stability, once the Nb_2O_5 was covered by sp^2 carbon, helping to solve the issue with respect to low electronic conductivity of Nb_2O_5; nevertheless, this carbon shell did not jeopardize pseudocapacitive properties. Subsequently, the symmetrical supercapacitors assembled with Ni_x : Al:MWCNT-Nb_2O_5 electrodes presented high capacitance, high energy – as it operated in 1.8 V – good stability – from shortened diffusion lengths for ion and electron transport along with large surface are in electrote/electrolyte interface – withstanding nearly 200,000 cycles. Along with this composite properties, the ESI deposition technique proved to be a simple and efficient method for mitigating the agglomeration of Nb_2O_5 nanoparticles; therefore, leading to easier electronic conduction. In sum, from the data reported, this carbon shell is a facile, low cost and efficient way to increase the electronic conductivity – keeping the structure intact and stable – enhancing also capacitance, energy density, and cycle stability. Additionally, as per expectation, the resistance of the device, after several thousand cycles increased; nonetheless, it presented good stability as well as withstood a number of cycles greater than usually published by the existing literature. Accordingly, this Ni_x : Al:MWCNT-Nb_2O_5 symmetrical supercapacitor has potential for large scale applications once it presented higher voltage operation than conventional aqueous one and high specific capacitance values.

Chapter 5

Future work

Many different adaptations, tests, and experiments were left for the future due to lack of time. Thus, below there here are some insights I would have appreciated trying during this masters program.

1. One question yet not fully understood by researchers is the H^+ insertion/extraction into WO_3 crystal lattice. Probably a three electrode system configuration or *in-situ* techniques may assist towards further elucidation;

2. Once tungsten deposited over copper forms what is known by literature as "*pseudo alloy*", a possibility is to grow W_2C:W_xO_y onto different substrates, and check whether different current collectors may provide superior capacitive behavior;

3. Try to employ the HFCVD for sublimation of different filaments, such as lanthanum;

4. Running Raman and XRD after cyclability in W_2C:W_xO_y composite in order to gather more data about the capacitance enhancement process, phase changes...;

5. Performing an analysis of NI_x : Al:MWCNT-Nb_2O_5 composite with three electrode system configuration;

6. Evaluate the performance of these composites in different electrolytes, such as organic, or ionic liquids.

Chapter 6

Conclusion

We reported transition metal oxides and carbide as electrodes for electrochemical capacitors. We presented a technique feasible for large scale production, employing environmentally friend composites as active materials. At first study, the W_2C:W_xO_y composite synthesized was performed by a facile method – HFCVD – that presented capacitance enhancements even after thousand of GCD cycles. It is worth noting that such aspect has outperformed published studies. Additionally, one of the W_2C:W_xO_y supercapacitors built self-improved its efficiency, as well as showed capacitance increase after 10,000 cycles due to pseudocapacitive behavior and proton insertion/extraction in WO_3 lattice. Regarding the other composite synthesized, named $Ni_xAl : MWCNT - Nb_2O_5$, it presented high capacitance and long lifespan – near 200,000 cycles of GCD – once it combined the stability and fast electron transport of MWCNT and carbon shell – achieved by calcination – and pseudocapacitive behavior from Nb_2O_5. In addition, the result was achieved due to an easy, low cost and large scale potential deposition technique known as electrospray ionization (ESI). Therefore, although the current study brings the synthesis of two distinct composites, they have similarities in respect of their nature – transition metal oxide metals with low cost – as well as the ability to provide long lifespan to the devices assembled, along with facile production techniques.

References

[1] A. González, E. Goikolea, J. A. Barrena, and R. Mysyk, "Review on supercapacitors: technologies and materials," *Renewable and Sustainable Energy Reviews*, vol. 58, pp. 1189–1206, 2016.

[2] B. E. Conway, *Electrochemical supercapacitors: scientific fundamentals and technological applications*. Springer Science & Business Media, 2013.

[3] A. J. Bard, L. R. Faulkner, J. Leddy, and C. G. Zoski, *Electrochemical methods: fundamentals and applications*, vol. 2. wiley New York, 1980.

[4] J. H. Chae, *Supercapacitors with neutral aqueous electrolytes*. PhD thesis, University of Nottingham, 2014.

[5] W. Nunes, R. Vicentini, L. M. Da Silva, L. H. Costa, T. Tadeu, and H. Zanin, "Surface and electrochemical properties of radially oriented multiwalled carbon nanotubes grown on stainless steel mesh," *Journal of The Electrochemical Society*, 2018.

[6] B. Tilak, C.-P. Chen, and S. Rangarajan, "A model to characterize the impedance of electrochemical capacitors arising from reactions of the type oad + n e- rad," *Journal of Electroanalytical Chemistry*, vol. 324, no. 1, pp. 405 – 414, 1992. An International Journal Devoted to all Aspects of Electrode Kinetics, Interfacial Structure, Properties of Electrolytes, Colloid and Biological Electrochemistry.

[7] M. Lu, *Supercapacitors: materials, systems, and applications*. John Wiley & Sons, 2013.

[8] H. Zanin, A. Peterlevitz, H. Ceragioli, R. Teófilo, F. Degasperi, V. Baranauskas, *et al.*, "Large-area cylindrical diamond electrodes," *ECS Journal of Solid State Science and Technology*, 2012.

[9] L. Yan, X. Rui, G. Chen, W. Xu, G. Zou, and H. Luo, "Recent advances in nanostructured nb-based oxides for electrochemical energy storage," *Nanoscale*, vol. 8, no. 16, pp. 8443–8465, 2016.

[10] A. Jaworek, "Electrospray droplet sources for thin film deposition," *Journal of materials science*, vol. 42, no. 1, pp. 266–297, 2007.

[11] L. L. Zhang and X. Zhao, "Carbon-based materials as supercapacitor electrodes," *Chemical Society Reviews*, vol. 38, no. 9, pp. 2520–2531, 2009.

[12] P. Simon and Y. Gogotsi, "Materials for electrochemical capacitors," *Nature materials*, vol. 7, no. 11, p. 845, 2008.

[13] C. McGlade and P. Ekins, "The geographical distribution of fossil fuels unused when limiting global warming to 2 c," *Nature*, vol. 517, no. 7533, p. 187, 2015.

[14] J. Gao, H. Hou, Y. Zhai, A. Woodward, S. Vardoulakis, S. Kovats, P. Wilkinson, L. Li, X. Song, L. Xu, *et al.*, "Greenhouse gas emissions reduction in different economic sectors: Mitigation measures, health co-benefits, knowledge gaps, and policy implications," *Environmental pollution*, vol. 240, pp. 683–698, 2018.

[15] C. B. Field, *Climate change 2014–Impacts, adaptation and vulnerability: Regional aspects*. Cambridge University Press, 2014.

[16] K. L. Ebi, N. H. Ogden, J. C. Semenza, and A. Woodward, "Detecting and attributing health burdens to climate change.," *Environmental health perspectives*, vol. 125, no. 8, pp. 085004–085004, 2017.

[17] E. G. Hertwich, T. Gibon, E. A. Bouman, A. Arvesen, S. Suh, G. A. Heath, J. D. Bergesen, A. Ramirez, M. I. Vega, and L. Shi, "Integrated life-cycle assessment of electricity-supply scenarios confirms global environmental benefit of low-carbon technologies," *Proceedings of the National Academy of Sciences*, vol. 112, no. 20, pp. 6277–6282, 2015.

[18] X. J. Yang, H. Hu, T. Tan, and J. Li, "China's renewable energy goals by 2050," *Environmental Development*, vol. 20, pp. 83–90, 2016.

[19] T. Jin and J. Kim, "What is better for mitigating carbon emissions–renewable energy or nuclear energy? a panel data analysis," *Renewable and Sustainable Energy Reviews*, vol. 91, pp. 464–471, 2018.

[20] S. Teleke, M. E. Baran, S. Bhattacharya, and A. Q. Huang, "Rule-based control of battery energy storage for dispatching intermittent renewable sources," *IEEE Transactions on Sustainable Energy*, vol. 1, no. 3, pp. 117–124, 2010.

[21] S. Saha, P. Samanta, N. C. Murmu, and T. Kuila, "A review on the heterostructure nanomaterials for supercapacitor application," *Journal of Energy Storage*, vol. 17, pp. 181–202, 2018.

[22] E. Azwar, W. A. W. Mahari, J. H. Chuah, D.-V. N. Vo, N. L. Ma, W. H. Lam, and S. S. Lam, "Transformation of biomass into carbon nanofiber for supercapacitor application–a review," *International Journal of Hydrogen Energy*, 2018.

[23] W. Raza, F. Ali, N. Raza, Y. Luo, E. E. Kwon, J. Yang, S. Kumar, A. Mehmood, and K.-H. Kim, "Recent advancements in supercapacitor technology," *Nano Energy*, 2018.

[24] J. R. Miller and P. Simon, "Electrochemical capacitors for energy management," *Science Magazine*, vol. 321, no. 5889, pp. 651–652, 2008.

[25] H. Yang, *Graphene-based supercapacitors for energy storage applications*. PhD thesis, The Ohio State University, 2013.

[26] Y. Gogotsi and V. Presser, *Carbon nanomaterials*. CRC press, 2013.

[27] A. Peterlevitz, P. May, R. Harniman, J. Jones, H. Ceragioli, and H. Zanin, "Fast electron transfer kinetics on novel interconnected nanospheres of graphene layers electrodes," *Thin Solid Films*, vol. 616, pp. 698–702, 2016.

[28] Q. Wei, F. Xiong, S. Tan, L. Huang, E. H. Lan, B. Dunn, and L. Mai, "Porous one-dimensional nanomaterials: design, fabrication and applications in electrochemical energy storage," *Advanced Materials*, vol. 29, no. 20, p. 1602300, 2017.

[29] B.-T. Liu, X.-M. Shi, X.-Y. Lang, L. Gu, Z. Wen, M. Zhao, and Q. Jiang, "Extraordinary pseudocapacitive energy storage triggered by phase transformation in hierarchical vanadium oxides," *Nature communications*, vol. 9, no. 1, p. 1375, 2018.

[30] W. Gong, B. Fugetsu, Z. Wang, I. Sakata, L. Su, X. Zhang, H. Ogata, M. Li, C. Wang, J. Li, *et al.*, "Carbon nanotubes and manganese oxide hybrid nanostructures as high performance fiber supercapacitors," *Communications Chemistry*, vol. 1, no. 1, p. 16, 2018.

[31] P. Simon, T. Brousse, and F. Favier, "Electrochemical double-layer capacitors (edlc)," *Supercapacitors Based on Carbon or Pseudocapacitive Materials*, pp. 1–25, 2017.

[32] H. Zanin, P. May, D. Fermin, D. Plana, S. Vieira, W. Milne, and E. Corat, "Porous boron-doped diamond/carbon nanotube electrodes," *ACS applied materials & interfaces*, vol. 6, no. 2, pp. 990–995, 2014.

[33] H. Zanin, E. Saito, H. Ceragioli, V. Baranauskas, and E. Corat, "Reduced graphene oxide and vertically aligned carbon nanotubes superhydrophilic films for supercapacitors devices," *Materials Research Bulletin*, vol. 49, pp. 487–493, 2014.

[34] M. Zogbi Jr, E. Saito, H. Zanin, F. Marciano, and A. Lobo, "Hydrothermal–electrochemical synthesis of nano-hydroxyapatite crystals on superhydrophilic vertically aligned carbon nanotubes," *Materials Letters*, vol. 132, pp. 70–74, 2014.

[35] R. Vicentini, L. H. Costa, W. Nunes, O. Vilas Boas, D. M. Soares, T. A. Alves, C. Real, C. Bueno, A. C. Peterlevitz, and H. Zanin, "Direct growth of mesoporous carbon on aluminum foil for supercapacitors devices," *Journal of Materials Science: Materials in Electronics*, pp. 1–10, 2018.

[36] P. Simon, T. Brousse, and F. Favier, *Supercapacitors Based on Carbon or Pseudocapacitive Materials*. 2017.

[37] V. Augustyn, J. Come, M. A. Lowe, J. W. Kim, P.-L. Taberna, S. H. Tolbert, H. D. Abruña, P. Simon, and B. Dunn, "High-rate electrochemical energy storage through li+ intercalation pseudocapacitance," *Nature materials*, vol. 12, no. 6, p. 518, 2013.

[38] C. Zhong, Y. Deng, W. Hu, J. Qiao, L. Zhang, and J. Zhang, "A review of electrolyte materials and compositions for electrochemical supercapacitors," *Chemical Society Reviews*, vol. 44, no. 21, pp. 7484–7539, 2015.

[39] F. Beguin and E. Frackowiak, *Carbons for electrochemical energy storage and conversion systems*. CRC Press, 2009.

[40] R. C. Alkire, Y. Gogotsi, and P. Simon, *Nanostructured materials in electrochemistry*. John Wiley & Sons, 2008.

[41] P. Cordoba-Torres, T. J. Mesquita, and R. P. Nogueira, "Relationship between the origin of constant-phase element behavior in electrochemical impedance spectroscopy and electrode surface structure," *The Journal of Physical Chemistry C*, vol. 119, no. 8, pp. 4136–4147, 2015.

[42] L. Gassa, J. Vilche, M. Ebert, K. Jüttner, and W. Lorenz, "Electrochemical impedance spectroscopy on porous electrodes," *Journal of Applied Electrochemistry*, vol. 20, no. 4, pp. 677–685, 1990.

[43] W.-F. Chen, J. T. Muckerman, and E. Fujita, "Recent developments in transition metal carbides and nitrides as hydrogen evolution electrocatalysts," *Chemical communications*, vol. 49, no. 79, pp. 8896–8909, 2013.

[44] T. Niu, "Old materials with new properties ii: The metal carbides," *Nano Today*, vol. 18, pp. 12 – 14, 2018.

[45] Y. Shi, I. Badran, and S. Mulmi, "Crystalline tantalum carbide and ditungsten carbide formation via hot wire chemical vapor deposition using the precursor of

1-methylsilacyclobutane," *Surface and Coatings Technology*, vol. 326, pp. 103–110, 2017.

[46] A. Baserga, V. Russo, F. Di Fonzo, A. Bailini, D. Cattaneo, C. Casari, A. L. Bassi, and C. Bottani, "Nanostructured tungsten oxide with controlled properties: Synthesis and Raman characterization," *Thin Solid Films*, vol. 515, no. 16, pp. 6465–6469, 2007.

[47] A. Kuzmin, J. Purans, E. Cazzanelli, C. Vinegoni, and G. Mariotto, "X-ray diffraction, extended x-ray absorption fine structure and Raman spectroscopy studies of wo3 powders and (1-x)wo3-y ' xreo2 mixtures," *Journal of Applied Physics*, vol. 84, no. 10, pp. 5515–5524, 1998.

[48] J. Chu, D. Lu, X. Wang, X. Wang, and S. Xiong, "Wo3 nanoflower coated with graphene nanosheet: Synergetic energy storage composite electrode for supercapacitor application," *Journal of Alloys and Compounds*, vol. 702, pp. 568–572, 2017.

[49] Y. Cai, Y. Wang, S. Deng, G. Chen, Q. Li, B. Han, R. Han, and Y. Wang, "Graphene nanosheets-tungsten oxides composite for supercapacitor electrode," *Ceramics International*, vol. 40, no. 3, pp. 4109–4116, 2014.

[50] K.-H. Chang, C.-C. Hu, C.-M. Huang, Y.-L. Liu, and C.-I. Chang, "Microwave-assisted hydrothermal synthesis of crystalline wo3–wo3 · 0.5 h2o mixtures for pseudocapacitors of the asymmetric type," *Journal of Power Sources*, vol. 196, no. 4, pp. 2387–2392, 2011.

[51] Z. Hai, M. K. Akbari, Z. Wei, C. Xue, H. Xu, J. Hu, and S. Zhuiykov, "Nano-thickness dependence of supercapacitor performance of the ald-fabricated two-dimensional wo3," *Electrochimica Acta*, vol. 246, pp. 625 – 633, 2017.

[52] C. P. P. Wong, K. M. Lee, and C. W. Lai, "Hydrothermal preparation of reduced graphene oxide/tungsten trioxide nanocomposites with enhanced electrochemical performance," *Journal of Materials Science: Materials in Electronics*, vol. 28, no. 19, pp. 14554–14567, 2017.

[53] N. M. Shinde, A. D. Jagadale, V. S. Kumbhar, T. R. Rana, J. Kim, and C. D. Lokhande, "Wet chemical synthesis of wo 3 thin films for supercapacitor application," *Korean Journal of Chemical Engineering*, vol. 32, no. 5, pp. 974–979, 2015.

[54] W. Sun, M. T. Yeung, A. T. Lech, C.-W. Lin, C. Lee, T. Li, X. Duan, J. Zhou, and R. B. Kaner, "High surface area tunnels in hexagonal wo3," *Nano Letters*, vol. 15, no. 7, pp. 4834–4838, 2015. PMID: 26075682.

[55] L. Erik and S. Wolf-Dieter, "Tungsten: properties, chemistry, technology of the element, alloys, and chemical compounds," 1999.

[56] T. L. Barr and S. Seal, "Nature of the use of adventitious carbon as a binding energy standard," *Journal of Vacuum Science & Technology A: Vacuum, Surfaces, and Films*, vol. 13, no. 3, pp. 1239–1246, 1995.

[57] V. Sittinger, M. Höfer, T. Harig, M. Justianto, H. Thiem, M. Vergöhl, and L. Schäfer, "Optical grade sio2 films prepared by hwcvd," *Surface and Coatings Technology*, 2017.

[58] A. Pflug, M. Höfer, T. Harig, M. Armgardt, C. Britze, M. Siemers, T. Melzig, and L. Schäfer, "Modeling of gas flow and deposition profile in hwcvd processes," *Thin Solid Films*, vol. 595, pp. 266–271, 2015.

[59] P. Chaudhari, N. Meshram, A. Singh, A. Topkar, and R. Dusane, "Hot wire chemical vapour deposition (hwcvd) of boron carbide thin films from ortho-carborane for neutron detection application," *Thin Solid Films*, vol. 519, no. 14, pp. 4561–4564, 2011.

[60] H. Umemoto, S. Setoguchi, H. Uemura, and H. Matsumura, "Coating techniques of metal chambers for remote catalytic chemical vapor deposition applications," *Journal of Vacuum Science & Technology A: Vacuum, Surfaces, and Films*, vol. 26, no. 2, pp. 309–311, 2008.

[61] C. Liang, F. Tian, Z. Wei, Q. Xin, and C. Li, "The synthesis of nanostructured w2c on ultrahigh surface area carbon materials via carbothermal hydrogen reduction," *Nanotechnology*, vol. 14, no. 9, p. 955, 2003.

[62] M. Gotić, M. Ivanda, S. Popović, and S. Musić, "Synthesis of tungsten trioxide hydrates and their structural properties," *Materials Science and Engineering: B*, vol. 77, no. 2, pp. 193–201, 2000.

[63] C. Liu, Y. Qiu, Y. Xia, F. Wang, X. Liu, X. Sun, Q. Liang, and Z. Chen, "Noble-metal-free tungsten oxide/carbon (wox/c) hybrid manowires for highly efficient hydrogen evolution," *Nanotechnology*, vol. 28, no. 44, p. 445403, 2017.

[64] I. Novoselova, S. Kuleshov, E. Fedoryshena, and V. Bykov, "Electrochemical synthesis of tungsten carbide in molten salts, its properties and applications," *ECS Transactions*, vol. 86, no. 14, pp. 81–94, 2018.

[65] J. Gabrusenoks, A. Veispals, A. Von Czarnowski, and K.-H. Meiwes-Broer, "Infrared and Raman spectroscopy of wo3 and cdwo4," *Electrochimica acta*, vol. 46, no. 13-14, pp. 2229–2231, 2001.

[66] J. Díaz-Reyes, V. Dorantes-García, A. Pérez-Benítez, and J. Balderas-López, "Obtaining of films of tungsten trioxide (wo3) by resistive heating of a tungsten filament," *Superficies y vacío*, vol. 21, no. 2, pp. 12–17, 2008.

[67] T. Kubo and Y. Nishikitani, "Deposition temperature dependence of optical gap and coloration efficiency spectrum in electrochromic tungsten oxide films," *Journal of the Electrochemical Society*, vol. 145, no. 5, pp. 1729–1734, 1998.

[68] P. Tägtström and U. Jansson, "Chemical vapour deposition of epitaxial wo3 films," *Thin Solid Films*, vol. 352, no. 1-2, pp. 107–113, 1999.

[69] A. S. Kurlov and A. I. Gusev, "Neutron and x-ray diffraction study and symmetry analysis of phase transformations in lower tungsten carbide w_2C," *Phys. Rev. B*, vol. 76, p. 174115, Nov 2007.

[70] W. Parrish, "Results of the iucr precision lattice-parameter project," *Acta Crystallographica*, vol. 13, no. 10, pp. 838–850, 1960.

[71] P. Woodward, A. Sleight, and T. Vogt, "Structure refinement of triclinic tungsten trioxide," *Journal of Physics and Chemistry of Solids*, vol. 56, no. 10, pp. 1305–1315, 1995.

[72] R. J. Colton and J. W. Rabalais, "Electronic structure to tungsten and some of its borides, carbides, nitrides, and oxides by x-ray electron spectroscopy," *Inorganic Chemistry*, vol. 15, no. 1, pp. 236–238, 1976.

[73] A. Katrib, F. Hemming, P. Wehrer, L. Hilaire, and G. Maire, "The multi-surface structure and catalytic properties of partially reduced wo3, wo2 and wc+ o2 or w+ o2 as characterized by xps," *Journal of electron spectroscopy and related phenomena*, vol. 76, pp. 195–200, 1995.

[74] L. A. Morimitsu, R. O. Ospina, J. G. Carmona, E. R. Parra, and P. A. Arango, "Deposition and computational analysis of wc thin films grown by papvd," *Revista Mexicana de Física*, vol. 59, no. 1, pp. 106–111, 2013.

[75] D. He, J. Pu, L. Wang, G. Zhang, Y. Wang, and Q. Xue, "Investigation of post-deposition annealing effects on microstructure, mechanical and tribological properties of wc/ac nanocomposite coatings," *Tribology Letters*, vol. 63, no. 2, p. 14, 2016.

[76] D. R. Stellwagen and J. H. Bitter, "Structure–performance relations of molybdenum- and tungsten carbide catalysts for deoxygenation," *Green Chemistry*, vol. 17, no. 1, pp. 582–593, 2015.

[77] G. Leclercq, M. Kamal, J. M. Giraudon, P. Devassine, L. Feigenbaum, L. Leclercq, A. Frennet, J. M. Bastin, A. Löfberg, S. Decker, *et al.*, "Study of the preparation of bulk powder tungsten carbides by temperature programmed reaction with ch4+ h2mixtures," *Journal of catalysis*, vol. 158, no. 1, pp. 142–169, 1996.

[78] F. P. Rouxinol, B. C. Trasferetti, R. Landers, and M. A. Moraes, "Hot-filament metal oxide deposition (HFMOD): a novel method for depositing thin films of metallic oxides," *Journal of the Brazilian Chemical Society*, vol. 15, no. 2, pp. 324–326, 2004.

[79] C. B. Rodella, D. H. Barrett, S. F. Moya, S. J. Figueroa, M. T. Pimenta, A. A. S. Curvelo, and V. T. da Silva, "Physical and chemical studies of tungsten carbide catalysts: effects of Ni promotion and sulphonated carbon," *RSC Advances*, vol. 5, no. 30, pp. 23874–23885, 2015.

[80] J. Jia, X. Liu, R. Mi, N. Liu, Z. Xiong, L. Yuan, C. Wang, G. Sheng, L. Cao, X. Zhou, *et al.*, "Self-assembled pancake-like hexagonal tungsten oxide with ordered mesopores for supercapacitors," *Journal of Materials Chemistry A*, vol. 6, no. 31, pp. 15330–15339, 2018.

[81] P. Biloen and G. Pott, "X-ray photoelectron spectroscopy study of supported tungsten oxide," *Journal of Catalysis*, vol. 30, no. 2, pp. 169–174, 1973.

[82] G. Mishra, G. C. Behera, S. Singh, and K. Parida, "Liquid phase esterification of acetic acid over WO_3 promoted β-sic in a solvent free system," *Dalton Transactions*, vol. 41, no. 47, pp. 14299–14308, 2012.

[83] D. Hachim, S. T. LoPresti, C. C. Yates, and B. N. Brown, "Shifts in macrophage phenotype at the biomaterial interface via il-4 eluting coatings are associated with improved implant integration," *Biomaterials*, vol. 112, pp. 95–107, 2017.

[84] R. A. Quinlan, Y.-C. Lu, D. Kwabi, Y. Shao-Horn, and A. N. Mansour, "Xps investigation of the electrolyte induced stabilization of $LiCoO_2$ and "$AlPO_4$"-coated $LiCoO_2$ composite electrodes," *Journal of The Electrochemical Society*, vol. 163, no. 2, pp. A300–A308, 2016.

[85] C. Sharan, P. Khandelwal, and P. Poddar, "The mechanistic insight into the biomilling of goethite (α-feo (oh)) nanorods using the yeast saccharomyces cerevisiae," *RSC Advances*, vol. 5, no. 111, pp. 91785–91794, 2015.

[86] Y.-L. Huang, H.-W. Tien, C.-C. M. Ma, S.-Y. Yang, S.-Y. Wu, H.-Y. Liu, and Y.-W. Mai, "Effect of extended polymer chains on properties of transparent graphene nanosheets conductive film," *Journal of Materials Chemistry*, vol. 21, no. 45, pp. 18236–18241, 2011.

[87] Y. Wang, X. Liao, Y. Luo, Q. Yang, and G. Li, "Influence of surface-functionalized graphene oxide on the cell morphology of poly (methyl methacrylate) composite," *Journal of Materials Science & Technology*, vol. 31, no. 5, pp. 463–466, 2015.

[88] S.-W. Jee, W. Choi, C. H. Ahn, G. Yang, H. K. Cho, J.-H. Lee, and C. Yu, "Enhanced oxygen reduction and evolution by in situ decoration of hematite nanoparticles on carbon nanotube cathodes for high-capacity nonaqueous lithium–oxygen batteries," *Journal of Materials Chemistry A*, vol. 3, no. 26, pp. 13767–13775, 2015.

[89] A. Shpak, A. Korduban, M. Medvedskij, and V. Kandyba, "Xps studies of active elements surface of gas sensors based on WO_{3-x} nanoparticles," *Journal of electron spectroscopy and related phenomena*, vol. 156, pp. 172–175, 2007.

[90] D. Barreca, S. Bozza, G. Carta, G. Rossetto, E. Tondello, and P. Zanella, "Structural and morphological analyses of tungsten oxide nanophasic thin films obtained by MOCVD," *Surface science*, vol. 532, pp. 439–443, 2003.

[91] S. Li, Z. Yao, J. Zhou, R. Zhang, and H. Shen, "Fabrication and characterization of wo3 thin films on silicon surface by thermal evaporation," *Materials Letters*, vol. 195, pp. 213–216, 2017.

[92] R. Ospina, E. Restrepo, Y. Arango, H. Castillo, and A. Devia, "Study of w/wc coatings varying the substrate temperature," in *AIP Conference Proceedings*, vol. 875, pp. 240–243, AIP, 2006.

[93] P. Swift, "Adventitious carbon—the panacea for energy referencing?," *Surface and Interface Analysis*, vol. 4, no. 2, pp. 47–51, 1982.

[94] D. Miller, M. Biesinger, and N. McIntyre, "Interactions of Co2 and CO at fractional atmosphere pressures with iron and iron oxide surfaces: one possible mechanism for surface contamination?," *Surface and Interface Analysis: An International Journal devoted to the development and application of techniques for the analysis of surfaces, interfaces and thin films*, vol. 33, no. 4, pp. 299–305, 2002.

[95] H. Piao and N. S. Mcintyre, "Adventitious carbon growth on aluminium and gold–aluminum alloy surfaces," *Surface and Interface Analysis: An International Journal devoted to the development and application of techniques for the analysis of surfaces, interfaces and thin films*, vol. 33, no. 7, pp. 591–594, 2002.

[96] L. Demarconnay, E. Raymundo-Piñero, and F. Béguin, "A symmetric carbon/carbon supercapacitor operating at 1.6 V by using a neutral aqueous solution," *Electrochemistry Communications*, vol. 12, no. 10, pp. 1275–1278, 2010.

[97] B. Liu, Y. Wang, H.-W. Jiang, and B.-X. Zou, "WO_3 nanowires on graphene sheets as negative electrode for supercapacitors," *Journal of Nanomaterials*, vol. 2017, 2017.

[98] K. Patel, C. Panchal, M. Desai, and P. Mehta, "An investigation of the insertion of the cations H^+, Na^+, K^+ on the electrochromic properties of the thermally evaporated WO_3 thin films grown at different substrate temperatures," *Materials Chemistry and Physics*, vol. 124, no. 1, pp. 884–890, 2010.

[99] M. B. Zellner and J. G. Chen, "Surface science and electrochemical studies of WC and W_2C PVD films as potential electrocatalysts," *Catalysis Today*, vol. 99, no. 3-4, pp. 299–307, 2005.

[100] X. Huang, H. Liu, X. Zhang, and H. Jiang, "High performance all-solid-state flexible micro-pseudocapacitor based on hierarchically nanostructured tungsten trioxide composite," *ACS applied materials & interfaces*, vol. 7, no. 50, pp. 27845–27852, 2015.

[101] H. Jiang, J. J. Hong, X. Wu, T. W. Surta, Y. Qi, S. Dong, Z. Li, D. P. Leonard, J. J. Holoubek, J. C. Wong, *et al.*, "Insights on the proton insertion mechanism in the electrode of hexagonal tungsten oxide hydrate," *Journal of the American Chemical Society*, vol. 140, no. 37, pp. 11556–11559, 2018.

[102] G. Orsini and V. Tricoli, "Fractal mesoporosity and proton transport in WO_3 xerogels," *J. Mater. Chem.*, vol. 22, pp. 23861–23870, 2012.

[103] K. Fic, G. Lota, M. Meller, and E. Frackowiak, "Novel insight into neutral medium as electrolyte for high-voltage supercapacitors," *Energy & Environmental Science*, vol. 5, no. 2, pp. 5842–5850, 2012.

[104] A. C. S. Valentim, E. O. da Silva, P. S. R. C. da Silva, D. S. Garcia, and M. I. B. Tavares, "Synergistic effect between hybrid nanoparticles of TiO_2 and Nb_2O_5 in the nanostructured materials based on EVA matrix," *Polymer Testing*, vol. 70, pp. 111–116, 2018.

[105] O. Lopes, V. Mendonça, F. Silva, E. Paris, and C. Ribeiro, "Óxidos de nióbio: uma visão sobre a síntese do Nb_2O_5 e sua aplicação em fotocatálise heterogênea," *Química Nova*, vol. 38, no. 1, pp. 106–117, 2015.

[106] T. Wang, Q. Le, J. Zhang, Y. Zhang, and W. Li, "Carbon cloth@ t-nb2o5@ mno2: A rational exploration of manganese oxide for high performance supercapacitor," *Electrochimica Acta*, vol. 253, pp. 311–318, 2017.

[107] H. Wen, Z. Liu, J. Wang, Q. Yang, Y. Li, and J. Yu, "Facile synthesis of Nb_2O_5 nanorod array films and their electrochemical properties," *Applied Surface Science*, vol. 257, no. 23, pp. 10084–10088, 2011.

[108] F. Kong, S. Tao, B. Qian, and L. Gao, "Multiwalled carbon nanotube-modified Nb_2O_5 with enhanced electrochemical performance for lithium-ion batteries," *Ceramics International*, vol. 44, no. 18, pp. 23226–23231, 2018.

[109] J. Y. Cheong, J.-W. Jung, D.-Y. Youn, C. Kim, S. Yu, S.-H. Cho, K. R. Yoon, and I.-D. Kim, "Mesoporous orthorhombic Nb_2O_5 nanofibers as pseudocapacitive electrodes with ultra-stable li storage characteristics," *Journal of Power Sources*, vol. 360, pp. 434–442, 2017.

[110] M. E. Lee, S. Y. Cho, H. J. Yoon, Y. S. Yun, and H.-J. Jin, "High-performance li-ion hybrid supercapacitors based on microporous pyropolymer nanoplates and orthorhombic Nb_2O_5 nanocomposites," *Journal of Industrial and Engineering Chemistry*, vol. 57, pp. 284–289, 2018.

[111] K. Kim, J. Hwang, H. Seo, H.-S. Kim, and J.-H. Kim, "Surface-controlled Nb_2O_5 nanoparticle networks for fast Li transport and storage," *Journal of Materials Science*, vol. 54, no. 3, pp. 2493–2500, 2019.

[112] M. Lübke, A. Sumboja, I. D. Johnson, D. J. Brett, P. R. Shearing, Z. Liu, and J. A. Darr, "High power nano-Nb_2O_5 negative electrodes for lithium-ion batteries," *Electrochimica Acta*, vol. 192, pp. 363–369, 2016.

[113] X. Wang, G. Li, Z. Chen, V. Augustyn, X. Ma, G. Wang, B. Dunn, and Y. Lu, "High-performance supercapacitors based on nanocomposites of Nb_2O_5 nanocrystals and carbon nanotubes," *Advanced Energy Materials*, vol. 1, no. 6, pp. 1089–1093, 2011.

[114] B. Anasori, M. Beidaghi, and Y. Gogotsi, "Graphene – transition metal oxide hybrid materials," *Materials Today*, vol. 17, no. 5, pp. 253 – 254, 2014.

[115] R. A. Rani, A. S. Zoolfakar, A. P. O'Mullane, M. W. Austin, and K. Kalantar-Zadeh, "Thin films and nanostructures of niobium pentoxide: fundamental properties, synthesis methods and applications," *Journal of Materials Chemistry A*, vol. 2, no. 38, pp. 15683–15703, 2014.

[116] F. Idrees, J. Hou, C. Cao, F. K. Butt, I. Shakir, M. Tahir, and F. Idrees, "Template-free synthesis of highly ordered 3D-hollow hierarchical Nb_2O_5 superstructures as an asymmetric supercapacitor by using inorganic electrolyte," *Electrochimica Acta*, vol. 216, pp. 332–338, 2016.

[117] E. Lim, H. Kim, C. Jo, J. Chun, K. Ku, S. Kim, H. I. Lee, I.-S. Nam, S. Yoon, K. Kang, *et al.*, "Advanced hybrid supercapacitor based on a mesoporous niobium pentoxide/carbon as high-performance anode," *ACS nano*, vol. 8, no. 9, pp. 8968–8978, 2014.

[118] J. W. Kim, V. Augustyn, and B. Dunn, "The effect of crystallinity on the rapid pseudocapacitive response of nb2o5," *Advanced Energy Materials*, vol. 2, no. 1, pp. 141–148, 2012.

[119] G. Li, X. Wang, and X. Ma, "Nb2o5-carbon core-shell nanocomposite as anode material for lithium ion battery," *Journal of Energy Chemistry*, vol. 22, no. 3, pp. 357–362, 2013.

[120] O. J. Fox, J. O. Holloway, G. M. Fuge, P. W. May, and M. N. Ashfold, "Electrospray deposition of diamond nanoparticle nucleation layers for subsequent CVD diamond growth," *MRS Online Proceedings Library Archive*, vol. 1203, 2009.

[121] L. Kong, C. Zhang, J. Wang, W. Qiao, L. Ling, and D. Long, "Nanoarchitectured nb 2 o 5 hollow, nb 2 o 5@ carbon and nbo 2@ carbon core-shell microspheres for ultrahigh-rate intercalation pseudocapacitors," *Scientific reports*, vol. 6, p. 21177, 2016.

[122] D. C. Harris, *Materials for infrared windows and domes: properties and performance*, vol. 70. SPIE press, 1999.

[123] R. B. Rakhi, B. Ahmed, M. N. Hedhili, D. H. Anjum, and H. N. Alshareef, "Effect of postetch annealing gas composition on the structural and electrochemical properties of Ti_2CT_x MXene electrodes for supercapacitor applications," *Chemistry of Materials*, vol. 27, no. 15, pp. 5314–5323, 2015.

[124] U. Balachandran and N. G. Eror, "Raman spectrum of the high temperature form of Nb_2O_5," *Journal of Materials Science Letters*, vol. 1, no. 9, pp. 374–376, 1982.

[125] A. A. McConnell, J. Aderson, and C. Rao, "Raman spectra of niobium oxides," *Spectrochimica Acta Part A: Molecular Spectroscopy*, vol. 32, no. 5, pp. 1067–1076, 1976.

[126] I. Mickova, "Photoelectrochemical study of anodically formed oxide films on niobium surfaces," *Croatica Chemica Acta*, vol. 83, no. 2, pp. 113–120, 2010.

[127] R. Brayner and F. Bozon-Verduraz, "Niobium pentoxide prepared by soft chemical routes: morphology, structure, defects and quantum size effect," *Physical Chemistry Chemical Physics*, vol. 5, no. 7, pp. 1457–1466, 2003.

[128] J. M. Jehng and I. E. Wachs, "Structural chemistry and Raman spectra of niobium oxides," *Chemistry of Materials*, vol. 3, no. 1, pp. 100–107, 1991.

[129] K. Bormanis, M. Palatnikov, O. Shcherbina, A. Frolov, P. Chufyrev, and N. Sidorov, "Physical properties and structure of niobium pentoxide ceramics treated by concentrated light flow," *Integrated Ferroelectrics*, vol. 123, no. 1, pp. 137–143, 2011.

[130] R. M. Pittman and A. T. Bell, "Raman studies of the structure of niobium oxide/titanium oxide (Nb_2O_5. TiO_2)," *The Journal of Physical Chemistry*, vol. 97, no. 47, pp. 12178–12185, 1993.

[131] B. X. Huang, K. Wang, J. S. Church, and Y.-S. Li, "Characterization of oxides on niobium by Raman and infrared spectroscopy," *Electrochimica acta*, vol. 44, no. 15, pp. 2571–2577, 1999.

[132] A. M. Raba, J. Bautista-Ruíz, and M. R. Joya, "Synthesis and structural properties of niobium pentoxide powders: A comparative study of the growth process," *Materials Research*, vol. 19, no. 6, pp. 1381–1387, 2016.

[133] L. G. Cançado, A. Jorio, E. M. Ferreira, F. Stavale, C. Achete, R. Capaz, M. Moutinho, A. Lombardo, T. Kulmala, and A. Ferrari, "Quantifying defects in graphene via Raman spectroscopy at different excitation energies," *Nano letters*, vol. 11, no. 8, pp. 3190–3196, 2011.

[134] E. Lim, C. Jo, H. Kim, M.-H. Kim, Y. Mun, J. Chun, Y. Ye, J. Hwang, K.-S. Ha, K. C. Roh, *et al.*, "Facile synthesis of Nb_2O_5@ carbon core–shell nanocrystals with controlled crystalline structure for high-power anodes in hybrid supercapacitors," *ACS nano*, vol. 9, no. 7, pp. 7497–7505, 2015.

[135] A. C. Ferrari and D. M. Basko, "Raman spectroscopy as a versatile tool for studying the properties of graphene," *Nature nanotechnology*, vol. 8, no. 4, p. 235, 2013.

[136] S. S. Rathore and S. Vitta, "Effect of divalent Ba cation substitution with Sr on coupled 'multiglass' state in the magnetoelectric multiferroic compound $Ba_3NbFe_3Si_2O_{14}$," *Scientific reports*, vol. 5, p. 9751, 2015.

[137] V. Nefedov, M. Firsov, and I. Shaplygin, "Electronic structures of $MRhO_2$, MRh_2O_4, $RhMO_4$ and Rh_2MO_6 on the basis of x-ray spectroscopy and ESCA data," *Journal of Electron Spectroscopy and Related Phenomena*, vol. 26, no. 1, pp. 65–78, 1982.

[138] N. Özer, M. D. Rubin, and C. M. Lampert, "Optical and electrochemical characteristics of niobium oxide films prepared by sol-gel process and magnetron sputtering a comparison," *Solar Energy Materials and Solar Cells*, vol. 40, no. 4, pp. 285–296, 1996.

[139] A. Gupta, M. Mittal, M. K. Singh, S. L. Suib, and O. P. Pandey, "Low temperature synthesis of nbc/c nano-composites as visible light photoactive catalyst," *Scientific reports*, vol. 8, 2018.

[140] V. Ivashchenko, P. Scrynskyy, O. Lytvyn, O. Butenko, O. Sinelnichenko, L. Gorb, F. Hill, J. Leszczynski, and A. Kozak, "Comparative investigation of NbN and Nb–Si–N films: Experiment and theory," *Journal of Superhard Materials*, vol. 36, no. 6, pp. 381–392, 2014.

[141] S. D. Jackson and J. S. Hargreaves, *Metal Oxide Catalysis, 2 Volume Set*, vol. 1. John Wiley & Sons, 2009.

[142] S. R. Sanivarapu, J. B. Lawrence, and G. Sreedhar, "Role of surface oxygen vacancies and lanthanide contraction phenomenon of $Nn(OH)_3$ (Ln = La, Pr, and Nd) in sulfide-mediated photoelectrochemical water splitting," *ACS Omega*, vol. 3, no. 6, pp. 6267–6278, 2018.

[143] B. Ullah, W. Lei, Z.-Y. Zou, X.-H. Wang, and W.-Z. Lu, "Synthesis strategy, phase-chemical structure and microwave dielectric properties of paraelectric $Sr_{(1-3x/2)}$ Ce_x TiO_3 ceramics," *Journal of Alloys and Compounds*, vol. 695, pp. 648–655, 2017.

[144] Y. Wang, C. Kang, D. Huang, K. Xiao, L. Zhu, F. Liu, and T. Tian, "Hydrothermal in situ synthesis of Rb and S co-doped Ti-based TiO2 sheet with a thin film showing high photocatalytic activities," *RSC Advances*, vol. 8, no. 20, pp. 11247–11254, 2018.

[145] L. David, S. Bernard, C. Gervais, P. Miele, and G. Singh, "Facile synthesis and high rate capability of silicon carbonitride/boron nitride composite with a sheet-like morphology," *The Journal of Physical Chemistry C*, vol. 119, no. 5, pp. 2783–2791, 2015.

[146] H. Ago, T. Kugler, F. Cacialli, W. R. Salaneck, M. S. Shaffer, A. H. Windle, and R. H. Friend, "Work functions and surface functional groups of multiwall carbon nanotubes," *The Journal of Physical Chemistry B*, vol. 103, no. 38, pp. 8116–8121, 1999.

[147] F. Castillejo, D. Marulanda, J. Olaya, and J. Alfonso, "Wear and corrosion resistance of niobium–chromium carbide coatings on AISI D2 produced through TRD," *Surface and Coatings Technology*, vol. 254, pp. 104–111, 2014.

[148] H. Nesbitt, D. Legrand, and G. Bancroft, "Interpretation of Ni2p XPS spectra of Ni conductors and Ni insulators," *Physics and Chemistry of Minerals*, vol. 27, no. 5, pp. 357–366, 2000.

[149] X. Li, H. Lei, C. Yang, and Q. Zhang, "Electrochemical fabrication of ultra-low loading Pt decorated porous nickel frameworks as efficient catalysts for methanol electro-oxidation in alkaline medium," *Journal of Power Sources*, vol. 396, pp. 64–72, 2018.

[150] L. Salvati Jr, L. E. Makovsky, J. Stencel, F. Brown, and D. M. Hercules, "Surface spectroscopic study of tungsten-alumina catalysts using X-ray photoelectron, ion scattering, and Raman spectroscopies," *The Journal of Physical Chemistry*, vol. 85, no. 24, pp. 3700–3707, 1981.

[151] N. Pegios, V. Bliznuk, S. Prünte, J. Schneider, R. Palkovits, and K. Simeonov, "Comparative study on la-promoted Ni/γ-Al_2O_3 for methane dry reforming–spray drying for enhanced nickel dispersion and strong metal–support interactions," *RSC Advances*, vol. 8, no. 2, pp. 606–618, 2018.

[152] D. L. Legrand, H. W. Nesbitt, and G. M. Bancroft, "X-ray photoelectron spectroscopic study of a pristine millerite (NiS) surface and the effect of air and water oxidation," *American Mineralogist*, vol. 83, no. 12, pp. 1256–1265, 1998.

[153] A. P. Grosvenor, M. C. Biesinger, R. S. C. Smart, and N. S. McIntyre, "New interpretations of XPS spectra of nickel metal and oxides," *Surface Science*, vol. 600, no. 9, pp. 1771–1779, 2006.

[154] B. Sasi and K. G. Gopchandran, "Nanostructured mesoporous nickel oxide thin films," *Nanotechnology*, vol. 18, p. 115613, feb 2007.

[155] B. Qiu, L. Cai, Y. Wang, Z. Lin, Y. Zuo, M. Wang, and Y. Chai, "Fabrication of nickel–cobalt bimetal phosphide nanocages for enhanced oxygen evolution catalysis," *Advanced Functional Materials*, vol. 28, no. 17, p. 1706008, 2018.

[156] P. Carraro, A. G. Blanco, G. Lener, D. Barrera, S. Amaya-Roncancio, C. Chanquía, H. Troiani, M. Oliva, and G. Eimer, "Nanostructured carbons modified with nickel as potential novel reversible hydrogen storage materials: Effects of nickel particle size," *Microporous and Mesoporous Materials*, vol. 273, pp. 50–59, 2019.

[157] O. Romanyuk, M. Varga, S. Tulic, T. Izak, P. Jiricek, A. Kromka, V. Skakalova, and B. Rezek, "Study of Ni-catalyzed graphitization process of diamond by in situ X-ray photoelectron spectroscopy," *The Journal of Physical Chemistry C*, vol. 122, no. 12, pp. 6629–6636, 2018.

[158] R. Thyagarajan, G. Cantin, B. Kashyap, and C. Bettles, "Modelling compaction behavior of nickel–phosphorus and nickel–boron electroless coated titanium powders," *Powder Technology*, vol. 274, pp. 53–61, 2015.

[159] L. Nie, A. Meng, J. Yu, and M. Jaroniec, "Hierarchically macro-mesoporous Pt/γ-Al_2O_3 composite microspheres for efficient formaldehyde oxidation at room temperature," vol. 3, p. 3215.

[160] B. J. Tan, K. J. Klabunde, and P. M. Sherwood, "XPS studies of solvated metal atom dispersed (smad) catalysts. evidence for layered cobalt-manganese particles on alumina and silica," *Journal of the American Chemical Society*, vol. 113, no. 3, pp. 855–861, 1991.

[161] S. H. Aboutalebi, A. T. Chidembo, M. Salari, K. Konstantinov, D. Wexler, H. K. Liu, and S. X. Dou, "Comparison of GO, GO/MWCNTs composite and MWCNTs as potential electrode materials for supercapacitors," *Energy & Environmental Science*, vol. 4, no. 5, pp. 1855–1865, 2011.

[162] E. Lim, C. Jo, M. S. Kim, M.-H. Kim, J. Chun, H. Kim, J. Park, K. C. Roh, K. Kang, S. Yoon, *et al.*, "High-performance sodium-ion hybrid supercapacitor based on Nb_2O_5@ carbon core–shell nanoparticles and reduced graphene oxide nanocomposites," *Advanced Functional Materials*, vol. 26, no. 21, pp. 3711–3719, 2016.

[163] H. Song, J. Fu, K. Ding, C. Huang, K. Wu, X. Zhang, B. Gao, K. Huo, X. Peng, and P. K. Chu, "Flexible Nb_2O_5 nanowires/graphene film electrode for high-performance hybrid Li-ion supercapacitors," *Journal of Power Sources*, vol. 328, pp. 599–606, 2016.

[164] L. Kong, C. Zhang, J. Wang, W. Qiao, L. Ling, and D. Long, "Free-standing T-Nb_2O_5/graphene composite papers with ultrahigh gravimetric/volumetric capacitance for li-ion intercalation pseudocapacitor," *ACS nano*, vol. 9, no. 11, pp. 11200–11208, 2015.

[165] Y. Guo, J. Li, M. Chen, and G. Gao, "Facile synthesis of vanadium pentoxide@ carbon core–shell nanowires for high-performance supercapacitors," *Journal of Power Sources*, vol. 273, pp. 804–809, 2015.

[166] L. bo Jiang, X. zhong Yuan, J. Liang, J. Zhang, H. Wang, and G. ming Zeng, "Nanostructured core-shell electrode materials for electrochemical capacitors," *Journal of Power Sources*, vol. 331, pp. 408 – 425, 2016.